JACS
JOURNAL OF THE AMERICAN CHEMICAL SOCIETY

Article

pubs.acs.org/JACS

Hybrid Germanium Iodide Perovskite Semiconductors: Active Lone Pairs, Structural Distortions, Direct and Indirect Energy Gaps, and Strong Nonlinear Optical Properties

Constantinos C. Stoumpos,[†] Laszlo Frazer,[‡] Daniel J. Clark,[§] Yong Soo Kim,[§,∥] Sonny H. Rhim,[‡,∥] Arthur J. Freeman,[‡] John B. Ketterson,[‡] Joon I. Jang,[§] and Mercouri G. Kanatzidis*[,†]

[†]Department of Chemistry, Northwestern University, Evanston, Illinois 60208, United States

[‡]Department of Physics and Astronomy, Northwestern University, Evanston, Illinois 60208, United States

[§]Department of Physics, Applied Physics and Astronomy, State University of New York (SUNY) at Binghamton, Binghamton, New York 13902, United States

[∥]Department of Physics and Energy Harvest-Storage Research Center, University of Ulsan, Ulsan 680-749, South Korea

Supporting Information

ABSTRACT: The synthesis and properties of the hybrid organic/inorganic germanium perovskite compounds, $AGeI_3$, are reported (A = Cs, organic cation). The systematic study of this reaction system led to the isolation of 6 new hybrid semiconductors. Using $CsGeI_3$ (**1**) as the prototype compound, we have prepared methylammonium, $CH_3NH_3GeI_3$ (**2**), formamidinium, $HC(NH_2)_2GeI_3$ (**3**), acetamidinium, $CH_3C(NH_2)_2GeI_3$ (**4**), guanidinium, $C(NH_2)_3GeI_3$ (**5**), trimethylammonium, $(CH_3)_3NHGeI_3$ (**6**), and isopropylammonium, $(CH_3)_2C(H)NH_3GeI_3$ (**7**) analogues. The crystal structures of the compounds are classified based on their dimensionality with **1**−**4** forming 3D perovskite frameworks and **5**−**7** 1D infinite chains. Compounds **1**−**7**, with the exception of compounds **5** (centrosymmetric) and **7** (nonpolar acentric), crystallize in polar space groups. The 3D compounds have direct band gaps of 1.6 eV (**1**), 1.9 eV (**2**), 2.2 eV (**3**), and 2.5 eV (**4**), while the 1D compounds have indirect band gaps of 2.7 eV (**5**), 2.5 eV (**6**), and 2.8 eV (**7**). Herein, we report on the second harmonic generation (SHG) properties of the compounds, which display remarkably strong, type I phase-matchable SHG response with high laser-induced damage thresholds (up to ∼3 GW/cm^2). The second-order nonlinear susceptibility, $\chi_S^{(2)}$, was determined to be 125.3 ± 10.5 pm/V (**1**), (161.0 ± 14.5) pm/V (**2**), 143.0 ± 13.5 pm/V (**3**), and 57.2 ± 5.5 pm/V (**4**). First-principles density functional theory electronic structure calculations indicate that the large SHG response is attributed to the high density of states in the valence band due to sp-hybridization of the Ge and I orbitals, a consequence of the lone pair activation.

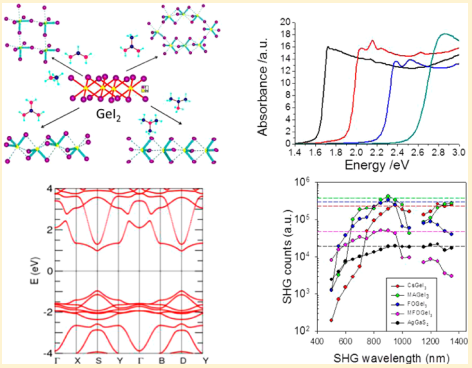

INTRODUCTION

In the past few years, the field of halide perovskites has been growing rapidly because of their unique optical and electronic properties. The class of halide perovskite compounds has a general formula of ABX_3, where A is a Cs^+, $CH_3NH_3^+$, or $HC(NH_2)_2^+$ cation; B is a Sn^{2+} or Pb^{2+} metal ion; and X^- is a halide anion. The major breakthrough that renewed the interest in this old class of compounds came in 2012 where both $CsSnI_3$[1] and $CH_3NH_3PbI_3$[2] were employed to fabricate high efficiency all-solid-state solar cells. Since then, a whole new era of solar energy research on halide perovskite compounds has emerged[3] with the efficiency record being close to 20%.[4] The popularity triggered by the successful implementation of the halide perovskites in solar energy research has also triggered the research interest in several other properties of the materials such as lasing,[5] radiation detection[6] and thermoelectric applications[7] or more subtle properties related to potential topological insulators[8] and Rashba splitting effect[9] stemming from the unique electronic structure of the compounds. The present work deals with the nonlinear optical (NLO) properties of the perovskite compounds focusing in the series of novel materials based on the much less studied Ge^{2+} metal ion. NLO materials are an actively pursued research topic because of their ability to generate coherent light at variable frequencies.[10] Second harmonic generation (SHG) is a key property that is the basis for a wide array of potential applications that span from laser manufacturing and engineering to living cell imaging in biosciences and various telecommunications and military applications.[11] For SHG, the prerequisite for the materials is the absence of a crystallographic inversion center in the structure.[12]

Received: January 29, 2015
Published: May 7, 2015

DOI: 10.1021/jacs.5b01025
J. Am. Chem. Soc. 2015, 137, 6804−6819

Previous efforts of our group have led to the discovery of the series of novel infrared (IR) SHG materials based on ternary and quaternary chalcogenide[13] and chalcophosphate[14] compounds. Our interest for the halide compounds presented here was triggered, however, by our recent work on hybrid iodide perovskites of Sn and Pb.[15] The Ge analogues differ from their heavier congeners because they show a pronounced tendency to crystallize in polar space groups.[16] This behavior of germanium iodides has been confirmed by other researchers[17] and has been acknowledged with a patent application.[18] We have elected the iodides over the lighter halides, which also produce strong SHG response,[19] since the largest size mismatch between Ge^{2+} and iodide is expected to give rise to much larger polarizability, and *ab initio* calculations bear out this hypothesis.[20]

Our current work reveals the remarkable optical properties of the germanium halide perovskites by replacing the inorganic cation in the A position of the perovskite unit with small polar organic molecules, leading to a class of hybrid perovskites, which is virtually unexplored.[21] The consequences of this substitution are dual. First, on structural grounds we find that the replacement of the alkali metal with a larger cation triggers the stereochemical expression of the $4s^2$ "inert pair" (also referred to as lone pair activation) which in turn triggers the modification of the band structure leading to a significant widening of the band gap. This increases the transparency region of the compounds in the visible region. Second, the polar nature of the organic cations causes them to orient inside the confined perovskite cage and results in a significant increase in the SHG response. The small organic cation substitution in polar compounds amplifies their SHG conversion efficiencies, as demonstrated here for the $AGeI_3$ system, and presumably can be further expanded to other structurally related systems containing a stereochemically active lone pair.

EXPERIMENTAL SECTION

Synthesis. $HC(NH_2)_2Cl$ (98%), $CH_3C(NH_2)_2Cl$ (98%), $C(NH_2)_3Cl$ (98%), $(CH_3)_3NHCl$ (98%), CsI (99.95%), and GeO_2 (99.999%) solids and distilled HI 57% (99.95%), H_3PO_2 50%, and CH_3NH_2 40% aqueous solutions, MeONa 25% methanolic solution and $(CH_3)_2C(H)NH_2$ were purchased from Sigma-Aldrich. $AgGaS_2$ and $AgGaSe_2$ were prepared using direct combination of the elements in evacuated fused silica ampules at 850 and 1050 °C, respectively.[22]

Orange GeI_4 was prepared from dissolution of GeO_2 in concentrated aqueous HI, and the solid thus obtained was recrystallized from hot toluene. CH_3NH_3I and $(CH_3)_2C(H)NH_3I$ were prepared by neutralizing equimolar amounts of HI and aqueous CH_3NH_2 and $(CH_3)_2C(H)NH_2$, respectively. $HC(NH_2)_2I$, $CH_3C(NH_2)_2I$, $C(NH_2)_3I$, and $(CH_3)_3NHI$ were prepared by neutralizing ethanolic solutions of $HC(NH)(NH_2)$, $CH_3C(NH)(NH_2)$, $C(NH)(NH_2)_2$, and $(CH_3)_3N$ (prepared by neutralizing the amidinium or ammonium chloride with sodium methoxide in EtOH and discarding NaCl) with aqueous HI, respectively. The purity of the materials was confirmed by powder X-ray diffraction (XRD).

General Procedure. A 2-neck flask was charged with a mixture of aqueous HI (6.8 mL, 7.58 M) and aqueous H_3PO_2 (3.4 mL, 9.14 M). The liquid was degassed by passing a stream of nitrogen through it for 1 min and keeping it under a nitrogen atmosphere throughout the experiment. GeI_4 (580 mg, 1 mmol) was dissolved in the mixture upon heating the flask to 120 °C using an oil bath, under constant magnetic stirring, forming a *bright* yellow solution. Direct addition of GeO_2 (105 mg, 1 mmol) in the solvent mixture still produces the bright yellow solution after ~30 min. A stoichiometric amount of the iodide salt was added to the solution resulting in the formation of the corresponding compound:

*$CsGeI_3$ (**1**).* To the above hot solution was added solid CsI (260 mg, 1 mmol) dissolving immediately. Five minutes after the addition of the solid a black solid started to precipitate. The stirring was discontinued and the solution was left to cool down to room temperature. *Black* truncated octahedral crystals were formed. The crystals were left to grow inside the mother liquor for 24 h under a nitrogen atmosphere before being filtered and washed with the minimum amount of degassed EtOH. Yield 80−90%. Energy-dispersive spectroscopy (EDS): Cs, 19.42% (20%); Ge, 18.20% (20%); I, 62.37% (60%).

*$CH_3NH_3GeI_3$ (**2**).* To above the hot solution was added solid CH_3NH_3I (159 mg, 1 mmol) dissolving immediately. The solution was evaporated to approximately half its original volume by heating at 120 °C. The stirring was discontinued, and the solution was left to cool down to room temperature. Upon cooling, *deep red*, elongated hexagonal plate-like crystals of the title compound were precipitated. The crystals were left to grow inside the mother liquor for 24 h under a nitrogen atmosphere before being filtered and washed with the minimum amount of degassed EtOH. Yield 80−90%. Diffuse reflectance infrared Fourier transform (DRIFT), KBr, cm^{-1}: 3182 br, 2708 w, 1579 s, 1467 s, 1246 m, 962 m, 906 s, 516 w, 403 w. EDS: Ge, 28.84% (25%); I, 71.16% (75%).

*$HC(NH_2)_2GeI_3$ (**3**).* To the above hot solution was added solid $HC(NH_2)_2I$ (172 mg, 1 mmol) dissolving immediately. The solution was evaporated to approximately half its original volume by heating at 120 °C. The stirring was discontinued, and the solution was left to cool down to room temperature. Upon cooling, *orange*, elongated hexagonal tubular crystals of the title compound were precipitated. The crystals were left to grow inside the mother liquor for 24 h under a nitrogen atmosphere before being filtered and washed with the minimum amount of degassed EtOH. Yield 80−90%. DRIFT, KBr, cm^{-1}: 3402 br, 3270 s, 1714 s, 1616 m, 1351 m, 1122 m, 1047 m, 588 s. EDS: Ge, 21.20% (25%); I, 78.80% (75%).

*$CH_3C(NH_2)_2GeI_3$ (**4**).* To the above hot solution was added solid $CH_3C(NH_2)_2I$ (184 mg, 1 mmol) dissolving immediately. The solution was evaporated to approximately half its original volume by heating at 120 °C. The stirring was discontinued, and the solution was left to cool down to room temperature. Upon cooling, *yellow*, elongated hexagonal tubular crystals of the title compound were precipitated. The crystals were left to grow inside the mother liquor for 24 h under a nitrogen atmosphere before being filtered and washed with the minimum amount of degassed EtOH. Yield 80−90%. DRIFT, KBr: 3402 br, 3270 s, 1714 s, 1616 m, 1351 m, 1122 m, 1047 m, 588s. EDS: Ge, 30.20% (25%); I, 69.80% (75%).

*$C(NH_2)_3GeI_3$ (**5**).* To the above hot solution was added solid $C(NH_2)_3I$ (183 mg, 1 mmol) dissolving immediately. The solution was evaporated to approximately half its original volume by heating at 120 °C. The stirring was discontinued, and the solution was left to cool down to room temperature. Upon cooling, *yellow*, elongated hexagonal tubular crystals of the title compound were precipitated. The crystals were left to grow inside the mother liquor for 24 h under a nitrogen atmosphere before being filtered and washed with the minimum amount of degassed EtOH. Yield 80−90%. DRIFT, KBr, cm^{-1}: 3402 br, 3270 s, 1714 s, 1616 m, 1351 m, 1122 m, 1047 m, 588 s. EDS: Ge, 22.36% (25%); I, 77.44% (75%).

*$(CH_3)_3NHGeI_3$ (**6**).* To the above hot solution was added solid $(CH_3)_3NHI$ (187 mg, 1 mmol) dissolving immediately. The solution was evaporated to approximately half its original volume by heating at 120 °C. The stirring was discontinued, and the solution was left to cool down to room temperature. Upon cooling, *pale yellow*, elongated hexagonal tubular crystals of the title compound were precipitated. The crystals were left to grow inside the mother liquor for 24 h under a nitrogen atmosphere before being filtered and washed with the minimum amount of degassed EtOH. Yield 80−90%. DRIFT, KBr, cm^{-1}: 3402 br, 3270 s, 1714 s, 1616 m, 1351 m, 1122 m, 1047 m, 588 s. EDS: Ge, 26.46% (25%); I, 73.54% (75%).

*$(CH_3)_2C(H)NH_3GeI_3$ (**7**).* To the above hot solution was added solid $(CH_3)_2C(H)NH_3I$ (187 mg, 1 mmol) dissolving immediately. The solution was evaporated to approximately half its original volume by heating at 120 °C. The stirring was discontinued, and the solution was left to cool down to room temperature. Upon cooling, *pale yellow*,

DOI: 10.1021/jacs.5b01025
J. Am. Chem. Soc. 2015, 137, 6804−6819

elongated hexagonal tubular crystals of the title compound were precipitated. The crystals were left to grow inside the mother liquor for 24 h under a nitrogen atmosphere before being filtered and washed with the minimum amount of degassed EtOH. Yield 80−90%. DRIFT, KBr, cm^{-1}: 3402 br, 3270 s, 1714 s, 1616 m, 1351 m, 1122 m, 1047 m, 588 s. EDS: Ge, 21.43% (25%); I, 78.57% (75%).

GeI_2 (8). In the absence of any added cation, when the above solution was evaporated to approximately half its original volume by heating at 120 °C, and subsequent cooling, *yellow*, very thin hexagonal plates of the title compound were precipitated. The crystals were filtered and washed with the minimum amount of degassed EtOH. Yield 60−70%. DRIFT, KBr, cm^{-1}: 3402 br, 3270 s, 1714 s, 1616 m, 1351 m, 1122 m, 1047 m, 588 s. EDS: Ge, 32.04% (33%); I, 68.96% (67%).

The purity of **1**−**8** was confirmed by powder XRD (Supporting Information Figures S1 and S2) and Raman spectroscopy. The compounds are stable in air for at least 12 h before the first signs of oxidation to GeI_4 could be detected. Therefore, sample preparation and characterization can be performed without any special precautions. Structural and spectroscopic data for $AgGaQ_2$ (Q = S, Se) are shown in Figure S3.

Powder X-ray Diffraction (XRD) Studies. Powder XRD measurements were performed using a silicon-calibrated CPS 120 INEL powder X-ray diffractometer (Cu Kα, 1.54056 Å, graphite monochromatized radiation) operating at 40 kV and 20 mA, equipped with a position-sensitive detector with a flat sample geometry.

Single Crystal XRD Studies. Single-crystal XRD experiments were performed using either a STOE IPDS II or IPDS 2T diffractometer using Mo Kα radiation (λ = 0.71073 Å) and operating at 50 kV and 40 mA. Integration and numerical absorption corrections were performed using the X-AREA, X-RED, and X-SHAPE programs. All structures were solved by direct methods and refined by full-matrix least-squares on F^2 using the SHELXTL program package.[23] The PLATON software,[24] embedded within the WINGX platform,[25] was used to identify the twinning domains and to confirm the correctness of the chosen space group. The "Structure Utilities" routine built within the Bilbao Crystallographic Server platform was used to navigate between the unit cells and the atomic coordinates of equivalent space groups and to determine group-subgroup relationships of the high symmetry space groups.[26]

Theoretical Calculations. First-principles calculations have been performed using full-potential linearized plane wave (FLAPW) method[27] with local-density approximation (LDA)[28] for the exchange-correlation potentials. Muffin-tin radii of 3.0 au (Cs), 2.35 au (Ge,I), 1.20 au (C,N), and 0.60 au (H) were used, where cutoffs for plane wave expansions and charge/potential representations were 20 and 196 Ry, respectively. For Brillouin zone summation, 35 × 35 × 35 mesh was used, which gave 3984, 11034, and 11034 κ points for $CsGeI_3$, $CH_3NH_3GeI_3$, and $HC(NH_2)_2GeI_3$ in the irreducible wedge, whereas 25 × 25 × 25 mesh was used for $CH_3C(NH_2)_2GeI_3$ with 4096 irreducible k points. The optical matrix elements were calculated using the so-called length-gauge formalism.[29]

RESULTS AND DISCUSSION

Synthesis and Structure Description. The synthesis of the perovskite halogermanate compounds **1**−**8** can be accomplished with a straightforward, scalable and reproducible approach that is based on precipitation of crystals from a hydriodic acid solution in the presence of a suitable reducing agent (H_3PO_2) to generate and stabilize the Ge^{2+} oxidation state in solution and to suppress formation of Ge^{4+}. Small organic cation salts were added to the solution to generate the desired $AGeI_3$ compounds. The size of the cations was varied incrementally starting from cesium in $CsGeI_3$ (**1**, a reference material) to methylammonium in $CH_3NH_3GeI_3$ (**2**) and formamidinium in $HC(NH_2)_2GeI_3$ (**3**) and then to a series of 4-atom cations with trigonal (pseudo)planar geometry. Thus, acetamidinium, guanidinium, trimethylammonium, and isopropylammonium were employed to prepare $CH_3C(NH_2)_2GeI_3$ (**4**), $C(NH_2)_3GeI_3$ (**5**), $(CH_3)_3NHGeI_3$ (**6**), and $(CH_3)_2C(H)NH_3GeI_3$ (**7**), respectively (Scheme 1). Finally, GeI_2 (**8**) was also prepared, by omitting the addition of a counterion salt in the HI solution, in order to be used as a control material with respect to the spectroscopic properties of the hybrid perovskites.

Scheme 1. Molecular Formulae of the A Cations Discussed in This Work

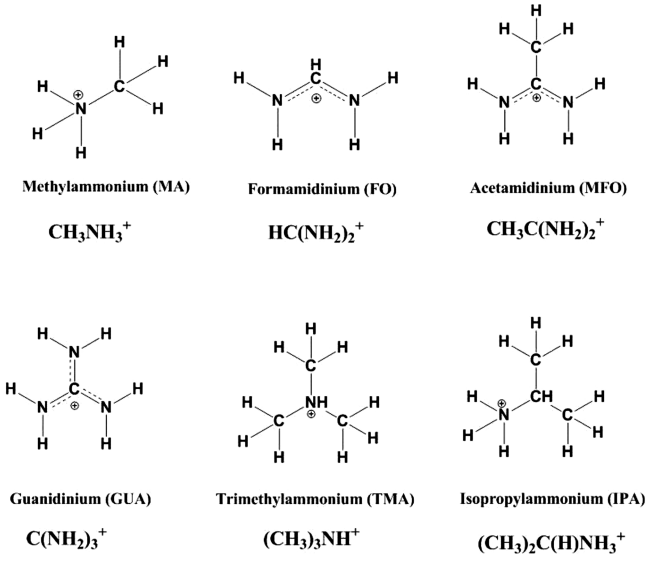

The crystal structures of the germanium iodides are generated by the assembly of trigonal pyramidal $[GeI_3]^-$ units wrapped around the A-cation spacers. The compounds are easily classified into three major categories, based on the connectivity of the $[GeI_3]^-$ building blocks in the structural framework (Figure 1).

The first category consists of 3D frameworks, assembled through single Ge−I−Ge bridges to form $[GeI_6]^{4-}$ corner-sharing octahedra. The octahedra adopt a trigonally distorted $CaTiO_3$ structure crystallizing in the polar $R3m$ space group. This structural type includes compounds **1**−**3** (Figure 1a−c) with the unit cell parameters increasing with the increase of the cation size (Table 1). The trigonal distortion causes loss of the 4-fold symmetry axes present in the aristotype cubic perovskite modification $Pm\bar{3}m$. For a given lattice parameter a, for the archetypal cubic perovskite, the unit cell is tripled in volume by the distortion adopting a trigonal unit cell with $\sqrt{2}a \times \sqrt{2}a \times \sqrt{3}a$ lattice parameters for a, b, and c axes, respectively. The distortion is enhanced by the presence of $CH_3NH_3^+$ which has an inherent C_{3v} symmetry and orients itself along the rhombohedral crystallographic c-axis. Interestingly, the $HC(NH_2)_2^+$ cation (C_{2v} symmetry) also orients itself along the 3-fold symmetry axis by aligning one C−N bond to the c-axis and disordering the second C−N bond about it, with an occupancy of 1/3. The net effect of this change is reflected in the Ge−I bond distances. The six Ge−I bonds in the octahedron split in three short ones and three long ones. The short bonds remain virtually constant at a distance of 2.73−2.77 Å for **1**−**3** so that the expansion of the unit cell with increasing cation volume is reflected in the long ones, Ge···I, which are regarded as weakly bonding interactions. These long bonds expand with increasing cation size from 3.26 Å in **1**, to 3.45 Å in **2** and to 3.58 in **3**.

DOI: 10.1021/jacs.5b01025
J. Am. Chem. Soc. 2015, 137, 6804−6819

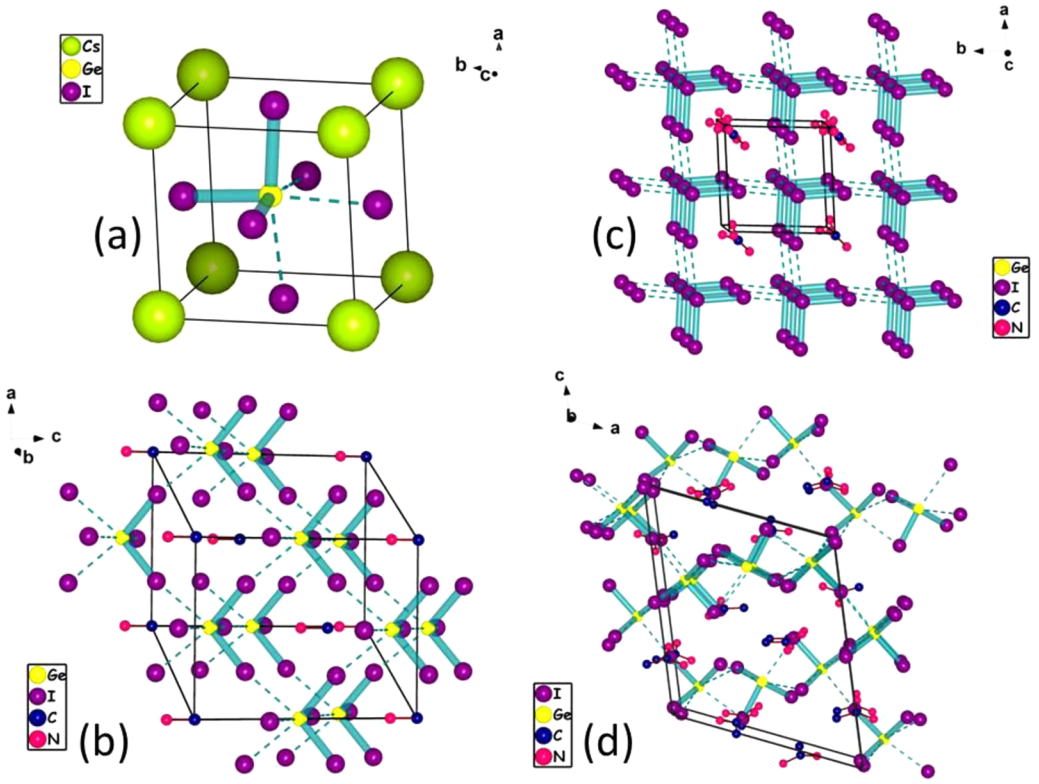

Figure 1. Crystal structures of the 3D germanium iodides. (a) The unit cell of $CsGeI_3$ (**1**) in the rhombohedral symmetry setting, (b) the unit cell of $CH_3NH_3GeI_3$ (**2**) in the hexagonal symmetry setting, (c) a 2 × 2 × 2 supercell of $HC(NH_2)_2GeI_3$ (**3**) in the rhombohedral symmetry setting, and (d) the unit cell of $CH_3C(NH_2)_2GeI_3$ (**4**). The dotted bonds indicate long contacts, while the thick bonds indicate covalent bonding. Note that the lattice parameters of the rhombohedral and hexagonal setting are related by the $a_R = a_H(\beta/3)$ (cell length) and $\alpha_R = 2$ arc $\sin(3/2\beta)$ (cell angle), where $\beta = (3 + (c_H/a_H)^2)^{1/2}$ and the R and H indices refer to the rhombohedral and octahedral cells, respectively.

Crystallographic data for **1**−**3** are given in Table 1 while full listings of the thermal and bonding parameters are provided in the Supporting Information.

A second structural type occurs when the size of the cation is such that it cannot be accommodated inside the 3D cavity of the cubic perovskite structure. As a result, the 3D framework collapses to give rise to the 1D hexagonal perovskite structure ($CsCdBr_3$-type) where the $[GeI_3]^-$ units are connected by Ge−I_3−Ge triple bridges forming $[GeI_6]^{4-}$ face-sharing octahedra that stack one behind another down a (pseudo)hexagonal axis. The A cations act as spacers between the chains in this structure type (Figure 2). This is a classic demonstration of the so-called counterion effect previously discussed extensively in metal chalcogenide frameworks.[30]

Thus, $C(NH_2)_3^+$, $(CH_3)_3NH^+$, and $(CH_3)_2C(H)NH_3^+$ cations force the construction of precisely this structural type in compounds **5**−**7**. However, despite the fact that the three compounds adopt the hexagonal perovskite structure, the assembly of the $[GeI_3]^-$ blocks is distinctly different among them. Thus, in $C(NH_2)_3GeI_3$ (**5**), the connectivity between the $[GeI_3]^-$ units occurs in an up−down fashion with respect to the chain-propagation axis, with one trigonal pyramid contributing two iodine atoms to the bridge and the adjacent $[GeI_3]^-$ unit, resulting in a centrosymmetric structure crystallizing in the $P2_1/c$ space group. This up−down configuration results in a deviation from linearity of the 1D chain with the Ge centers oscillating above and below the ideal orientation axis. On the other hand, $(CH_3)_3NHGeI_3$ (**6**) adopts a more regular conformation with the $[GeI_3]^-$ pyramids stacking one behind the other down the crystallographic 6-fold and 3-fold screw axes leading to a noncentrosymmetric structure crystallizing in the $P6_3$ space group. The last compound in this family $(CH_3)_2C(H)NH_3GeI_3$ (**7**) crystallizes in the tetragonal space group $I\bar{4}2d$ and consists of 1D chains of $[GeI_3]^-$ building blocks stacking collinearly. The chains span perpendicular to the 4-fold symmetry axis in two different orientations which are perpendicular to one another and related through diamond glide symmetry. The compound shows a large degree of modulation with approximately 3/4 of the reflections displaying streaking and diffuse scattering along the [100] and [010] directions in reciprocal space (Figure S4). For this reason, the structure was refined as disordered with the iodine atoms occupying two positions relative to the ordered germanium atoms at 2.6 and 3.6 Å, respectively.

In the case of $CH_3(NH_2)_2GeI_3$ (**4**), an intermediate crystal structure arises falling between the two extremes (Figure 1d). Thus, $CH_3(NH_2)_2GeI_3$ crystallizes in a quasi-3D pseudohexagonal crystal structure crystallizing in the monoclinic space group $P2_1$. The crystal structure consists of face-sharing $[Ge_3I_9]^{3-}$ linear building blocks, very similar to those observed in $C(NH_2)_3GeI_3$, but in contrast to $C(NH_2)_3GeI_3$, these blocks are further connected to one another in corner-sharing fashion through weak bonding interactions, which resemble the connectivity pattern observed in **1**−**3**. As a result, hexagonal cavities of $[Ge_3I_9]^{3-}$ units form encapsulating three $CH_3(NH_2)_2^+$ cations. This distinctively contrasts the 3D perovskite arrangement of **1**−**3** where the arrangement $[GeI_3]^-$ units result in the formation of a distorted cubic cavity accommodating a single cation. Crystallographic data for **4**−**7** are given in Table 2.

DOI: 10.1021/jacs.5b01025
J. Am. Chem. Soc. 2015, 137, 6804−6819

Table 1. Crystallographic Data and Refinement Details for 1−3[a]

compound	1	2	3
Chemical formula	$CsGeI_3$	$CH_3NH_3GeI_3$	$HC(NH_2)_2GeI_3$
Formula weight	586.20	485.36	498.36
Refinement method		Full-matrix least-squares on F^2	
Temperature		293(2) K	
Wavelength		0.71073 Å	
Crystal system	Trigonal	Trigonal	Trigonal
Space group	*R*3m	*R*3m	*R*3m
Unit cell dimensions	a = 8.3582(11) Å,	a = 8.5534(13) Å,	a = 8.4669(15) Å,
	α = 90.00°	α = 90.00°	α = 90.00°
	b = 8.3582(11) Å,	b = 8.5534(13) Å,	b = 8.4669(15) Å,
	β = 90.00°	β = 90.00°	β = 90.00°
	c = 10.6098(15) Å,	c = 11.162(2) Å,	c = 11.729(2) Å,
	γ = 120.00°	γ = 120.00°	γ = 120.00°
Volume (Å^3)	641.89(15)	707.2(2)	728.2(2)
Z	3	3	3
$\rho_{(calc)}$ (g/cm^3)	4.549	3.419	3.409
μ (mm^{-1})	18.484 mm^{-1}	12.983 mm^{-1}	12.616 mm^{-1}
F(000)	738	630	648
Crystal size (mm^3)	0.085 × 0.041 × 0.027	0.057 × 0.031 × 0.018	0.108 × 0.039 × 0.034
θ range	3.41 to 29.12°	3.30 to 29.05°	3.28 to 29.15°
Index ranges	$-11 \le h \le 11$,	$-9 \le h \le 10$,	$-11 \le h \le 11$,
	$-11 \le k \le 11$,	$-11 \le k \le 11$,	$-10 \le k \le 11$,
	$-13 \le l \le 14$	$-15 \le l \le 15$	$-15 \le l \le 15$
Refl. collected	2057	2203	2214
Independent refl.	454 [R_{int} = 0.0410]	506 [R_{int} = 0.0359]	508 [R_{int} = 0.0508]
Completeness to θ	100%	98.5%	96.3%
Data/restr./param.	454/1/15	506/1/16	508/3/19
Goodness-of-fit	1.232	1.366	1.112
Final R indices [$>2\sigma(I)$]	R_{obs} = 0.0273,	R_{obs} = 0.0366,	R_{obs} = 0.0270,
	wR_{obs} = 0.0586	wR_{obs} = 0.0533	wR_{obs} = 0.0485
R indices [all data]	R_{all} = 0.0278,	R_{all} = 0.0382,	R_{all} = 0.0332,
	wR_{all} = 0.0587	wR_{all} = 0.0536	wR_{all} = 0.0510
2nd twin domain	[-1−1 0 0 1 0 0 0−1]	[-1−1 0 0 1 0 0 0−1]	[-1−1 0 0 1 0 0 0−1]
	3(5) %	3(5) %	8(5) %
Extinction coefficient	0.0152(6)	0.0027(3)	0.0063(7)
Largest diff. peak and hole (e·Å^{-3})	1.480 and −0.744	0.668 and −0.774	0.592 and −0.552

[a] $R = \sum||F_o| - |F_c||/\sum|F_o|$, $wR = \{\sum[w(|F_o|^2 - |F_c|^2)^2]/\sum[w(|F_o|^4)]\}^{1/2}$ and calc $w = 1/[\sigma^2(F_o^2) + (0.0362P)^2 + 0.0000P]$ where $P = (F_o^2 + 2F_c^2)/3$.

The trend observed in **1**−**7** suggests a strong dependence on the cation size. For **1**−**3**, the Cs^+, $CH_3NH_3^+$, and $HC(NH_2)_2^+$ cations are small enough to stabilize the distorted cubic perovskite structure. The increase in the cation size within **1**−**3** is transcribed in the $[GeI_3]^-_\infty$ inorganic lattice as a rhombohedral distortion of the ideal cubic perovskite cage. As the alkylammonium cation increases in size for the 4-atom cations (excluding H atoms), a breakdown of the 3D lattice occurs and instead the self-assembly of the iodogermanate units dictates a 1D (pseudo)hexagonal structural arrangement. However, there is no obvious size dependence for the 4-atom cations, and the most important parameter governing the crystal structure type appears to be the position of the amine/imine group in the cation. Thus, for the amidines $CH_3(NH_2)_2GeI_3$ and $C(NH_2)_3GeI_3$, the imine functional groups impose the formation of zigzag $[Ge_3I_9]^{3-}$ trimers that, depending on their further connectivity, result in 3D (in $CH_3(NH_2)_2GeI_3$) or 1D (in $C(NH_2)_3GeI_3$) crystal structure. On the other hand, the ternary amine in $(CH_3)_3NHGeI_3$ and the bulky primary amine in $(CH_3)_2C(H)NH_3GeI_3$ tend to favor a linear stacking of $[GeI_3]^-$ pyramids resulting in 1D structural types. As in the case of the cubic perovskites **1**−**3**, the internal symmetry of the organic cation appears to strongly influence the symmetry of the inorganic lattice in $(CH_3)_3NHGeI_3$ and $(CH_3)_2C(H)NH_3GeI_3$.

Optical Properties of the Compounds. *1. Band Gaps.* In accordance with the dimensional reduction of the inorganic lattice in **1**−**8**, the color of the compounds gradually changes from black in $CsGeI_3$ to pale yellow in $(TMAGeI_3)$. The parent compound, GeI_2, is bright yellow. The optical absorption, measured in a diffuse reflectance mode,[31] is in excellent agreement with colors confirming that the compounds are medium-to-wide gap semiconductors with band gaps ranging from 1.6 eV in $CsGeI_3$ to 2.8 eV in $TMAGeI_3$ (Figure 3). In the 3D compounds **1**−**4**, the band gap increases systematically by an impressively large 0.3 eV when the relatively small Cs^+ cation is replaced by the bulkier MA (1.9 eV), FO (2.2 eV), and MFO (2.5 eV) cations. We attribute this remarkable feature to the association of $[GeI_3]^-$ pyramids to form the $[GeI_6]^{4-}$ octahedra within the perovskite structure. The polyhedra have a C_{3v} local symmetry and generate two sets of Ge−I bonds (see Table 3). The three short bonds, which for **1**−**4** are within the narrow 2.73−2.78 Å range, define the pyramidal subunits. On the other hand, the three long bonds span a much

DOI: 10.1021/jacs.5b01025
J. Am. Chem. Soc. 2015, 137, 6804−6819

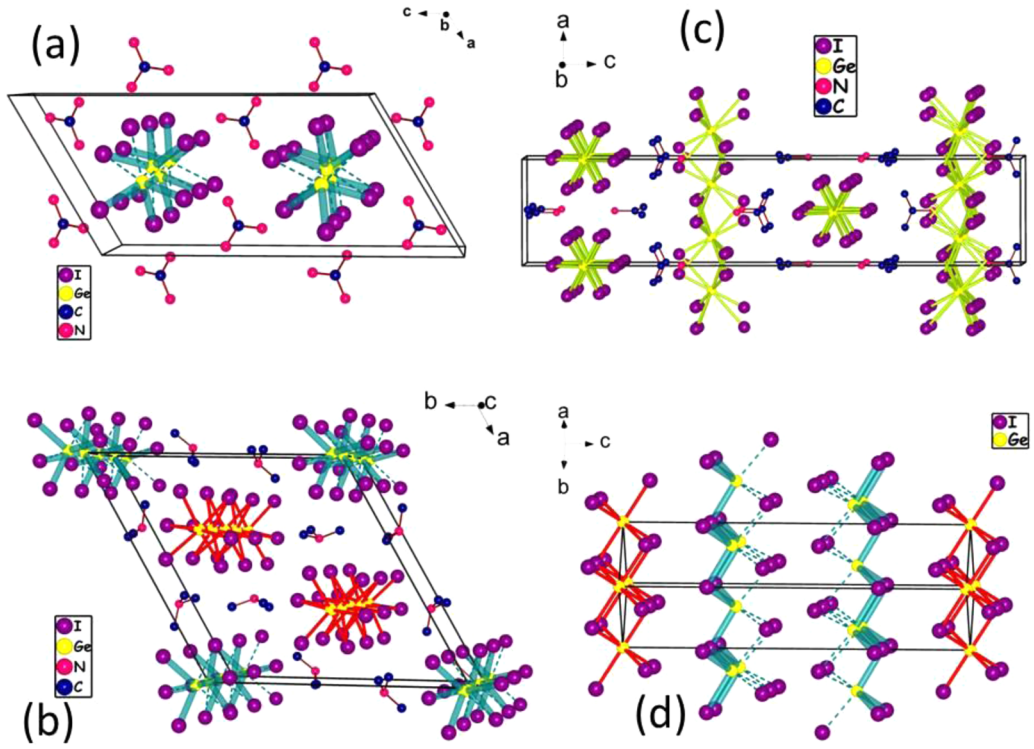

Figure 2. Crystal structures of the 1D and 2D germanium iodides. Unit cells of (a) $C(NH_2)_3GeI_3$ (**5**), (b) $(CH_3)_3NHGeI_3$ (**6**), (c) $(CH_3)_2C(H)NH_3GeI_3$ (**7**), and (d) GeI_2 (**8**). The dotted bonds indicate weaker long contacts, while the thick bonds indicate covalent bonding. Bonding color code: cyan, trigonal pyramidal bond; red, octahedral connectivity; green, disordered connectivity.

wider range starting from 3.26 Å in $CsGeI_3$ to 3.60 Å in $MFOGeI_3$ and define the connectivity of the perovskite lattice. Thus, the increase of the band gap in the optical spectrum from $CsGeI_3$ through $MFOGeI_3$ reflects the incremental spatial separation of the $[GeI_3]^-$ units leading to weaker orbital overlap which gives narrow bandwidths and therefore larger band separation. The absorption edge in **1**−**4** is sharp, suggesting a direct band gap, which has been previously confirmed in the case of $CsGeI_3$ by means of *ab initio* calculations,[20b] and also from theoretical calculations reported here (vide infra).

On the other hand, the 1D perovskites **5**−**7** display a much wider band gap between 2.7 and 2.8 eV which appears to be spectrally broad, suggesting an indirect gap transition. Particularly in the case of $IPAGeI_3$, there is a large band tail close to the optical absorption edge which is most likely related to the structural disorder associated with the compound. The layered binary compound, GeI_2 (**8**), has an intermediate direct band gap between the two extremes at 2.4 eV.[32] Compound $MFOGeI_3$ also appears to lie in between, effectively representing the bridge between the two structural types behaving as a quasi-3D compound. Tauc plots of the absorption, obtained by plotting the absorption coefficient α as α^2 (for direct gap) and as $\sqrt{\alpha}$ (for indirect gap) vs the radiation energy seem to agree with the above assignments, although it needs to be mentioned that some degree of absorption occurs below the direct gap, which is probably associated with some degree of structural disorder in the compounds (Figure S5).[33]

In an attempt to correlate the measured linear optical properties of the compounds with their respective structural characteristics, we examined the bond length and bond angle variations between the $[GeI_3]^-$ pyramidal units. For the assessment of the bond distance contribution to the band gap, we define a *g*-parameter, where $g = (b - a)/(a + b)$, where *a* refers to the short, covalent Ge−I bond distance and *b* refers to the long bond Ge···I distance (see Structure discussion above). Therefore, the *g*-parameter defines the degree of distortion of the GeI_6 octahedron in the perovskite structure. For the evaluation of the impact of the Ge−I−Ge bond angle on the band gap, we separated the angles in two different categories: (i) the corner-sharing angle, which connects two $[GeI_3]^-$ units through a single iodide ion (**1**−**4**) and (ii) the face-sharing angle, which connects two $[GeI_3]^-$ units through three iodide ions (**4**−**8**). The results are summarized in Figure 3c, d. From the above analysis, a clear trend emerges, showing a nearly linear increase of the band gap with increasing separation of the $[GeI_3]^-$ units and the concomitant decrease of the bonding Ge−I−Ge angle for the 3D compounds **1**−**4**. The band gaps of the 1D compounds **5**−**7** on the other hand do not display any significant dependence on the bond angle.

2. Crystal Symmetry through Nonlinear Optical and Vibrational Spectroscopy. With the exception of $GUAGeI_3$, compounds **1**−**7** crystallize in noncentrosymmetric space groups and are expected to have SHG response. The SHG property was initially measured under 1064 nm (Nd:YAG) excitation to check the crystal symmetry. The binary compound, GeI_2 (**8**), has also been examined in terms of SHG activity and rather surprisingly it exhibited a clear (albeit weak) response, despite the fact that the crystal structure of the compounds is reported as centrosymmetric ($P\bar{3}m1$ space group).[34] We attribute weak response to stacking faults, as it is well-known that compounds of the CdI_2-structure type are very prone to show such defects due to the weak van der Waals interactions between the layers. Thus, the SHG properties of GeI_2 will not be further discussed. The relative SHG intensities

DOI: 10.1021/jacs.5b01025
J. Am. Chem. Soc. 2015, 137, 6804−6819

Table 2. Crystallographic Data and Refinement Details for 4−7[a]

compound	4	5	6	7 (average)
Chemical formula	$CH_3C(NH_2)_2GeI_3$	$C(NH_2)_3GeI_3$(5)	$(CH_3)_3NHGeI_3$	$(CH_3)_2C(H)NH_3GeI_3$
Formula weight	512.39	513.40	513.41	513.41
Refinement method	Full-matrix least-squares on F^2			
Temperature	293(2) K			
Wavelength	0.71073 Å			
Crystal system	Monoclinic	Monoclinic	Hexagonal	Tetragonal
Space group	$P2_1$	$P2_1/c$	$P6_3$	$I\text{-}42d$
Unit cell dimensions	a = 12.5627(5) Å, α = 90.00°	a = 9.2308(9) Å, α = 90.00°	a = 15.9457(13) Å, α = 90.00°	a = 7.9004(3) Å, α = 90.00°
	b = 9.3403(4) Å, β = 112.996(3)°	b = 7.3399(4) Å, β = 120.650(8)°	b = 15.9457(13) Å, β = 90.00°	b = 7.9004(3) Å, β = 90.00°
	c = 14.8345(7) Å, γ = 90.00°	c = 17.974(2) Å, γ = 90.00°	c = 7.7504(7) Å, γ = 120.00°	c = 36.988(2) Å, γ = 90.00°
Volume (Å^3)	1602.34(12)	1047.65(17)	1706.6(2)	2308.64(19)
Z	6	4	6	8
$\rho_{(calc)}$ (g/cm^3)	3.186	3.255	2.997	2.954
μ (mm^{-1})	11.472	11.726	10.77	10.614
F(000)	1344	1040	1356	1808
Crystal size (mm^3)	0.171 × 0.059 × 0.037	0.098 × 0.056 × 0.035	0.193 × 0.041 × 0.034	0.0815 × 0.0636 × 0.0335
θ range	1.76 to 29.15°	2.57 to 29.12°	2.55 to 29.28°	2.20 to 24.92°
Index ranges	$-17 \le h \le 16$, $-12 \le k \le 12$, $-20 \le l \le 20$	$-11 \le h \le 12$, $-10 \le k \le 8$, $-22 \le l \le 24$	$-19 \le h \le 21$, $-21 \le k \le 18$, $-10 \le l \le 10$	$-9 \le h \le 9$, $-9 \le k \le 8$, $-43 \le l \le 40$
Refl. collected	15502	4781	11760	7466
Independent refl.	8593 [R_{int} = 0.0248]	2744 [R_{int} = 0.0441]	3082 [R_{int} = 0.0779]	1019 [R_{int} = 0.1009]
Completeness to θ	99.4%	97.2%	98.9%	100%
Data/restr./param	8593/1/209	2744/0/74	3082/4/56	1019/0/42
Goodness-of-fit	0.940	1.077	1.060	1.254
Final R indices [$>2\sigma(I)$]	R_{obs} = 0.0270, wR_{obs} = 0.0518	R_{obs} = 0.0412, wR_{obs} = 0.1031	R_{obs} = 0.0692, wR_{obs} = 0.1692	R_{obs} = 0.0825, wR_{obs} = 0.1439
R indices [all data]	R_{all} = 0.0370, wR_{all} = 0.0539	R_{all} = 0.0500, wR_{all} = 0.1074	R_{all} = 0.1076, wR_{all} = 0.1922	R_{all} = 0.1018, wR_{all} = 0.1526
2nd twin domain	-	-	[-1 0 0 1 1 0 0 0−1] 30.2(3)%	[1 0 0 0−1 0 0 0 1] 10(35)%
3rd twin domain	[-1 0 0 0−1 0 0 0−1] 15(1)%	-	[-1 0 0 0−1 0 0 0−1] 23(8)%	N/A
4th twin domain	-	-	[1 0 0 1−1 0 0 0 1] 19.8(3)%	-
Extinction coeff.	0.00320(8)	0.0214(9)	-	-
Largest diff. peak and hole (e·Å^{-3})	0.873 and −0.710	1.064 and −1.114	3.242 and −2.648	0.646 and −1.155

[a] $R = \sum||F_o| - |F_c||/\sum|F_o|$, $wR = \{\sum[w(|F_o|^2 - |F_c|^2)^2]/\sum[w(|F_o|^4)]\}^{1/2}$ and calc $w = 1/[\sigma^2(F_o^2) + (0.0362P)^2 + 0.0000P]$ where $P = (F_o^2 + 2F_c^2)/3$.

of the **1**−**8** scaled against the $AgGaSe_2$ reference are summarized in Table 3.

Since at 532 nm (2.33 eV) most of the compounds, including the reference, are not transparent to the produced SHG radiation, we conducted a wavelength-dependence study of **1**−**7** in order to better observe the SHG and to assess in what extent self-absorption affects the SHG output. Before moving to the full characterization of the SHG properties of the compounds, it was deemed necessary to identify all possible spectral transitions (electronic and vibrational ones) in order to determine the broadband transparency ranges of **1**−**7** in the 400−25 000 nm region (visible and IR domains). Thus, broadband absorption measurements were carried out using a diffuse reflectance setup (Figure S6).

Obviously, the upper limit for all compounds comes at (or close to) the band gap but the lower limit in **2**−**7** is governed by the absorption of the organic cations present in the hybrid materials. Normally, this is expected to occur at the mid-IR region, mainly through C−H vibrations, between 3000 and 5000 nm. However, due to combinations and overtones of the fundamental absorptions, the lower limit of transparency is practically decreased to ∼1400 nm (Figure S6). Effectively, these overtones interfere with the excitation beam and negatively impact the SHG output.

The limits can be grouped and generalized in terms of the functional groups for each cation. Thus, amidines ($FOGeI_3$, $MFOGeI_3$, and $GUAGeI_3$) are limited to 1400 nm and primary amines ($MAGeI_3$ and $IPAGeI_3$) are limited to 2100 nm, while the tertiary amine ($TMAGeI_3$) shows a broader transparency region. Surprisingly, the Cs^+ analogue ($CsGeI_3$) also displays a strong absorption at 2700 nm, the origin of which is not clearly understood at this point, although a similar absorption has been also observed in the isostructural compound $CsGeBr_3$[19c] This mid-IR absorption is rather unusual for a medium gap inorganic semiconductor, as exemplified by $AgGaSe_2$ having optical transparency up to 18 000 nm. Since the measured SHG

DOI: 10.1021/jacs.5b01025
J. Am. Chem. Soc. 2015, 137, 6804−6819

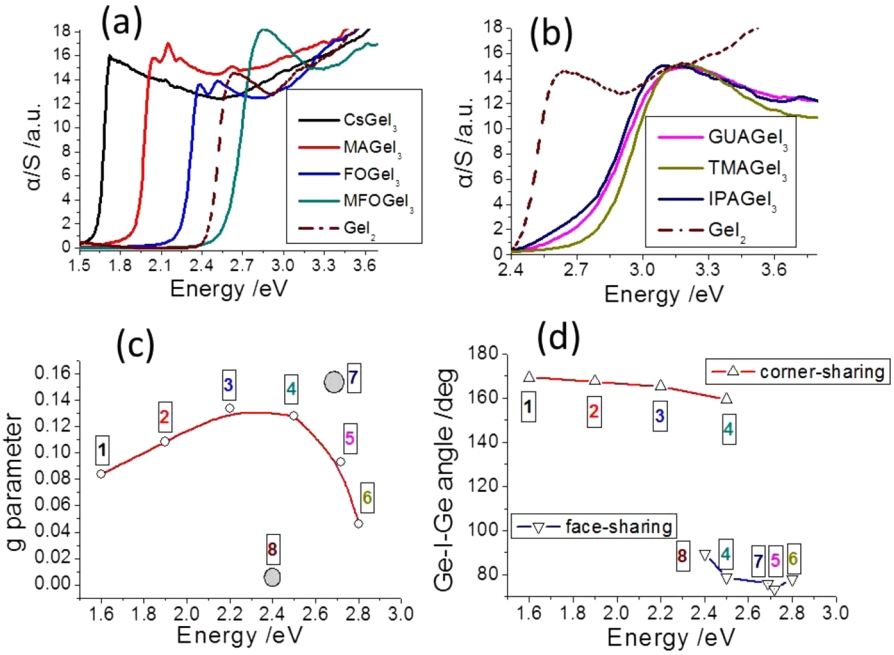

Figure 3. Optical absorption spectra of **1**−**8**. (a) The absorption spectra of the 3D compounds **1**−**4**, each showing a sharp absorption edge corresponding to a direct band gap and (b) the absorption spectra of the 1D compounds **5**−**7**, each showing a relatively broad absorption edge corresponding to an indirect gap. The absorption of the 2D binary compound **8** (GeI_2) is shown for reference as a dashed line. (c) Plot of the bonding g-parameter (defined in the text) as a function of band gap for **1**−**8**. The solid red line serves as a guide to the eye. $IPAGeI_3$and GeI_2 deviate from the line due to disorder and octahedral coordination, respectively, and are marked with gray circles. (d) Plot of Ge−I−Ge as a function of band gap for **1**−**8**. The corner-sharing and face-sharing labels refer to the connectivity of the GeI_3^- pyramids. $MFOGeI_3$ appears in both lines due to mixed connectivity. The solid red and blue lines serve as a guide to the eye.

Table 3. Linear and Nonlinear Optical Properties of 1−7 Together with the Ge−I Bonding Distances

compound	Ge−I bond length[a] (Å)	E_g(eV)	refractive index (at E_g)[b]	SHG intensity (532 nm) vs $AgGaSe_2$[c]	transparency range (μm)
$CsGeI_3$ (**1**)	2.753, 3.256	1.6	2. 78	40	2.68−0.78
$MAGeI_3$ (**2**)	2.772, 3.446	1.9	2.66	200	2.10−0.65
$FOGeI_3$ (**3**)	2.733, 3.577	2.2	2.56	12500	1.43−0.56
$MFOGeI_3$ (**4**)	2.784, 3.601 ⟨2.750⟩, ⟨3.572⟩	2.5	2.48	22000	1.43−0.50
$GUAGeI_3$ (**5**)	⟨2.793⟩, ⟨3.365⟩	2.7	2.44	-	1.43−0.47
$TMAGeI_3$ (**6**)	2.872, 3.332 ⟨3.019⟩, ⟨3.100⟩ ⟨2.991⟩, ⟨3.130⟩	2.8	2.41	30	2.28−0.44
$IPAGeI_3$ (**7**)	⟨2.654⟩, ⟨3.633⟩	2.7	2.43	4	2.10−0.47
GeI_2 (**8**)	2.865, 2.811, 3.140	2.4	2.50	1	83−0.52

[a]Values in brackets denote average bond lengths. [b]The refractive indices were estimated using the expression n^4E_g = 95 eV.[48] [c]The values are provided for a relative comparison at 532 nm for 137.5 ± 12.5 μm. The SHG efficiencies for narrow-gap materials were highly suppressed due to absorption at this wavelength.

properties of $CsGeI_3$ are not affected by this absorption (vide infra) within our experimental range, no further studies were carried out in the context of the present work.

Raman spectra of the perovskites were recorded in the range 100−2000 cm^{-1} with the aim of gaining further insight on the local symmetry of **1**−**8** and to verify the purity of the measured samples in terms of oxidation (Figure 4). Compounds **1**−**7** are spectroscopically pure in contrast to the readily oxidizable GeI_2. The oxidation-product is GeI_4, and in the case of GeI_2, it almost always coexists (as confirmed also by powder XRD data, Figure S2). The ternary iodide compounds appear to resist such a conversion which becomes measurable only when the materials are left exposed in air overnight.

For the analysis of the vibrational modes, the compounds were treated as interacting $[GeI_3]^-$ pyramids rather than $[GeI_6]^{4-}$ octahedra. In such a configuration, there are four Raman-active modes: ν_1 and ν_3, which are the stretching modes, and ν_2 and ν_4, which are the bending modes. Throughout the series of compounds, only the stretching modes were observed with the exception of **5** where all four modes can be assigned. The vibrational frequencies are in good agreement with reported values of related compounds[35] and are given in Table 4.

Taking compound $CsGeI_3$ as an example, the lowest energy peak at 127 cm^{-1} corresponds to the antisymmetric stretching ν_3 and displays the highest scattering intensity followed by the symmetric stretching ν_1 at 179 cm^{-1}. As one progresses from

DOI: 10.1021/jacs.5b01025
J. Am. Chem. Soc. 2015, 137, 6804−6819

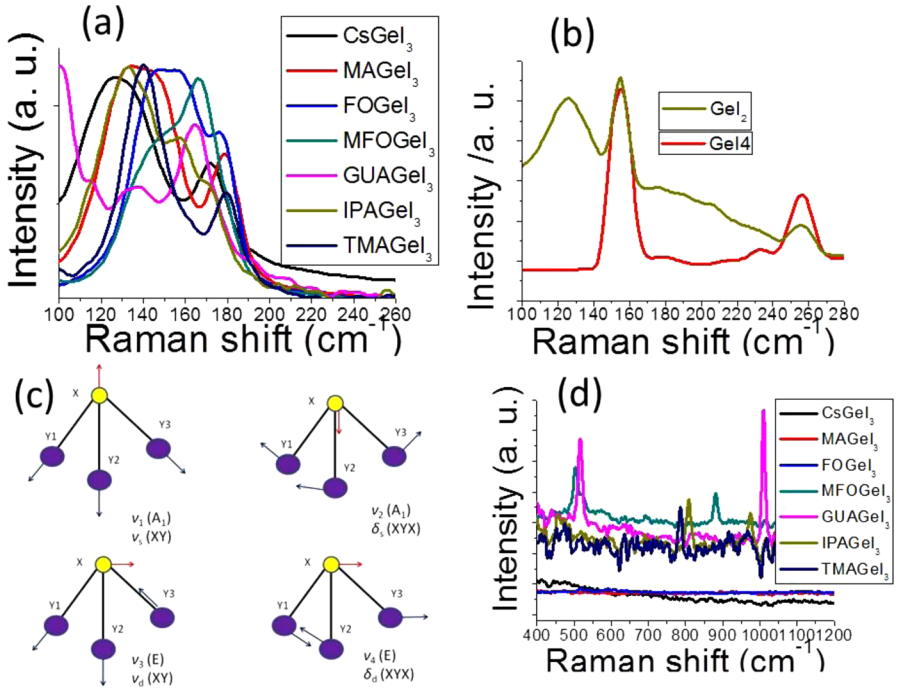

Figure 4. FT-Raman spectra of **1**–**8**. (a) Compounds **1**–**7** and (b) GeI_2 and GeI_4 in the 100–260 cm^{-1} range. (c) A schematic of the active vibrational modes of the $[GeI_3]^-$ pyramids.(d) Compounds **1**–**7** in the 400–1200 cm^{-1} range showing the contribution of the organic cations in the spectrum.

Table 4. Raman Scattering Properties of 1–8

compound	ν_1 (cm^{-1})	ν_2 (cm^{-1})	ν_3 (cm^{-1})	ν_4 (cm^{-1})	ν_3/ν_1 (intensity)	$\lvert\nu_3 - \nu_1\rvert$ (cm^{-1})
$CsGeI_3$ (**1**)	172	-	127	-	1.61	45
$MAGeI_3$ (**2**)	179	-	134, 145	-	1.58	39
FO_2GeI_3 (**3**)	176	-	148, 157	-	1.36	23
$MFOGeI_3$ (**4**)	166	-	150	-	0.77	16
$GUAGeI_3$ (**5**)	165	115	137	101	0.83	28
$TMAGeI_3$ (**6**)	180	-	140	-	1.55	40
$IPAGeI_3$ (**7**)	158, 171	-	133, 141	-	2.18	28
GeI_2 (**8**)	126	-	126	-	1	0
GeI_4	155	-	256	-	2.35	101

the simplest compound, GeI_2 (**8**), where both modes merge due to the equivalence of the Ge–I bond distances (effectively octahedral coordination), to the ternary compounds where the modes split into individual ones (effectively pyramidal coordination), two characteristic trends can be observed. The first one is that ν_1 gains while ν_3 loses in energy converging to one another. The second one is that ν_1 gains in intensity with respect to ν_3. This is particularly true for **1**–**4** and interestingly these four compounds display the largest degree of polarity. This trend is also in excellent agreement with structural considerations in **1**–**4** where the intrapyramidal Ge–I distances remain practically constant, whereas the interpyramidal ones become larger in the order $CsGeI_3$ < $MAGeI_3$ < $FOGeI_3$ < $MFOGeI_3$.

On the contrary, no such trend can be seen for the 1D compounds, although it is interesting that $GUAGeI_3$, the only centrosymmetric compound, displays all four vibration modes, including the bending ones.

The polar organic cations themselves also show a trend following the weakening of the C–N bond strength in the TMA < IPA < GUA < MFO order. Although MA and FO display their characteristic peaks at 475 and 517 cm^{-1}, respectively, those are very weak in intensity. Apparently, the only visible signature of these two cations in the Raman spectra is the splitting in the ν_3 mode of the Ge–I stretching (Table 4). For the compounds **2**–**7**, the fundamental peaks appear to be both IR- (Figure S6) and Raman-active (Figure 4) *except* for $GUAGeI_3$, thus confirming through the rule of mutual exclusion that $GUAGeI_3$ is a centrosymmetric compound.

3. Broadband SHG Properties. Our preliminary NLO screening (Table 4) showed that compounds **1**–**4** are highly SHG active. To obtain more quantitative results from compounds **1**–**4**, broadband SHG measurements were conducted for 7 different particle sizes employing the powder method.[36] We first measured the broadband SHG properties of the $AGeI_3$ samples as a function of λ = 1000–2700 nm; the corresponding SHG range is $\lambda/2$ = 500–1350 nm (see Figure 5). To produce seamless SHG response, we did not use any band-pass filter. We confirmed that there was no SHG signal from the capillary tube holding the sample and other optical components in our experimental range. The SHG responses of $AGeI_3$ were directly compared with those from a phase-matching reference material, $AgGaS_2$,[37] because **1**–**4** are all type-I phase-matchable (Figure 6) and have similar refractive

DOI: 10.1021/jacs.5b01025
J. Am. Chem. Soc. 2015, 137, 6804–6819

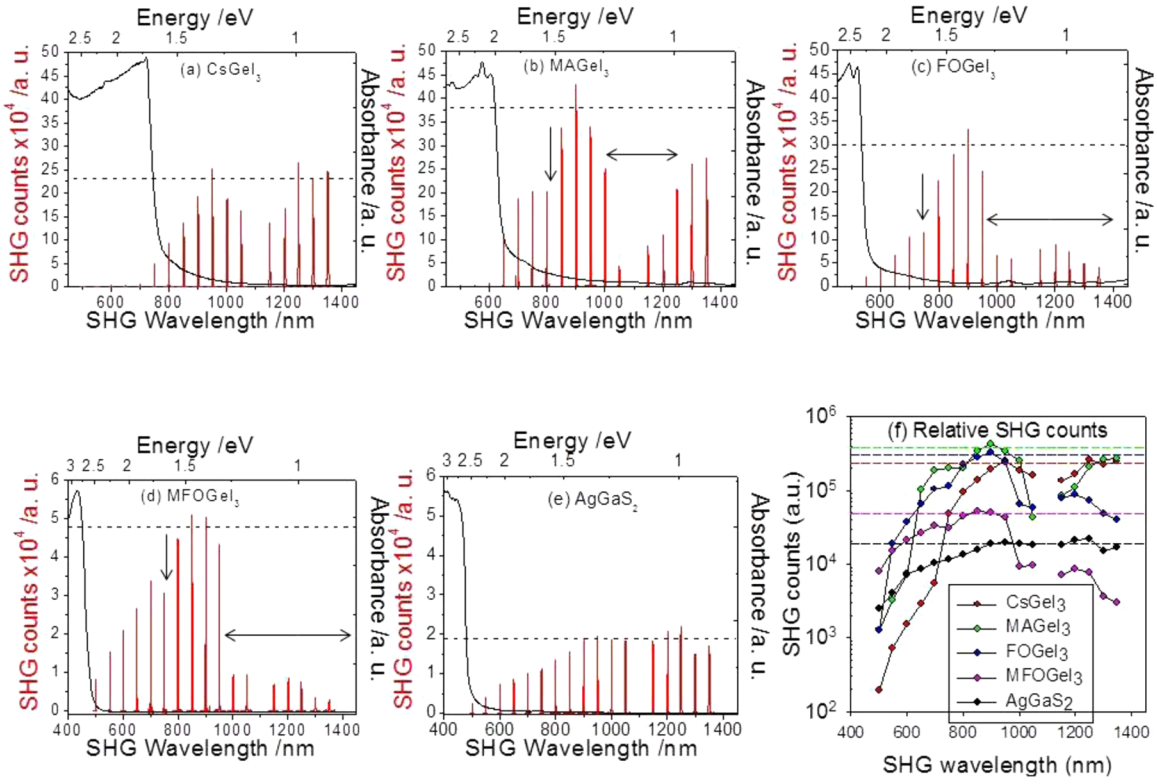

Figure 5. λ-dependent SHG scans for (a) $CsGeI_3$, (b) $MAGeI_3$, (c) $FOGeI_3$, (d) $MFOGeI_3$, and (e) $AgGaS_2$. The dashed lines roughly indicate the predicted SHG counts in the static limit and the arrows for the linear absorption ranges. The absorption edge for each compound has been drawn (black line) for comparison purposes. (f) Semilog plot of relative SHG counts.

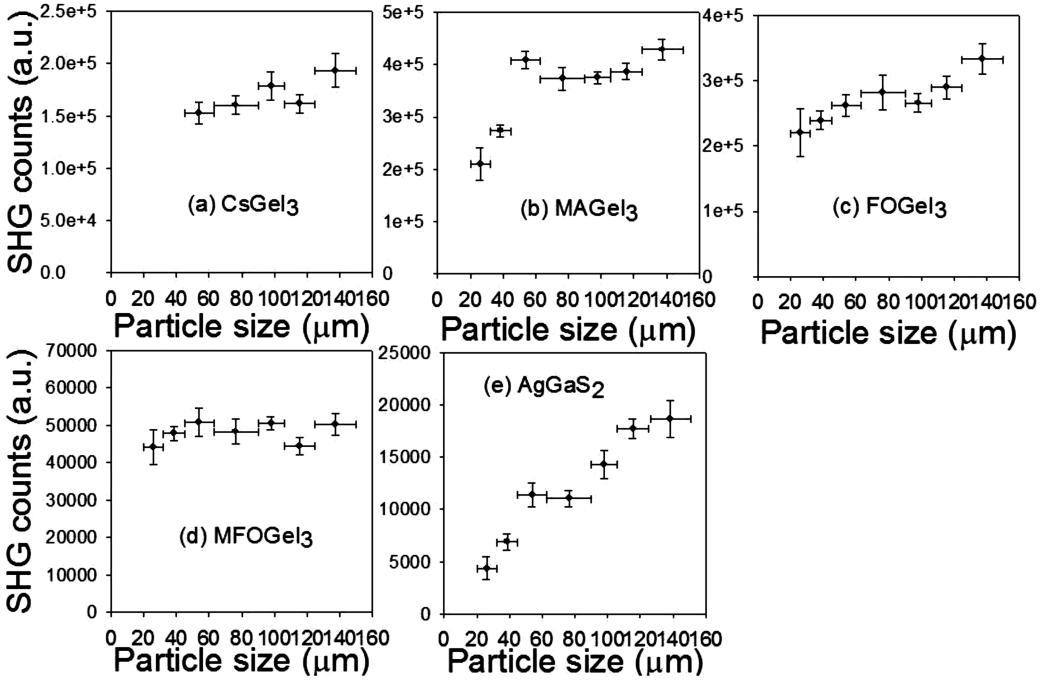

Figure 6. SHG particle size dependence of (a) $CsGeI_3$, (b) $MAGeI_3$, (c) $FOGeI_3$, (d) $MFOGeI_3$, and (e) $AgGaS_2$ at λ = 1800 nm, respectively, showing type-I phase matching.

indices (Table 3). The assignment is based on their increasing SHG intensity with increasing particle size, thus satisfying the criteria for type-I phase-matching.[36] This result is also consistent with previous studies for $AGeX_3$ compounds (where A is a monovalent cation and X is Cl, Br or I),[19,38] including $CsGeI_3$.[17c]

The series of red traces in Figure 5a shows the observed SHG spectra from powders of $CsGeI_3$ as λ varies in our experimental range. The sharp decrease in the observed SHG

DOI: 10.1021/jacs.5b01025
J. Am. Chem. Soc. 2015, 137, 6804−6819

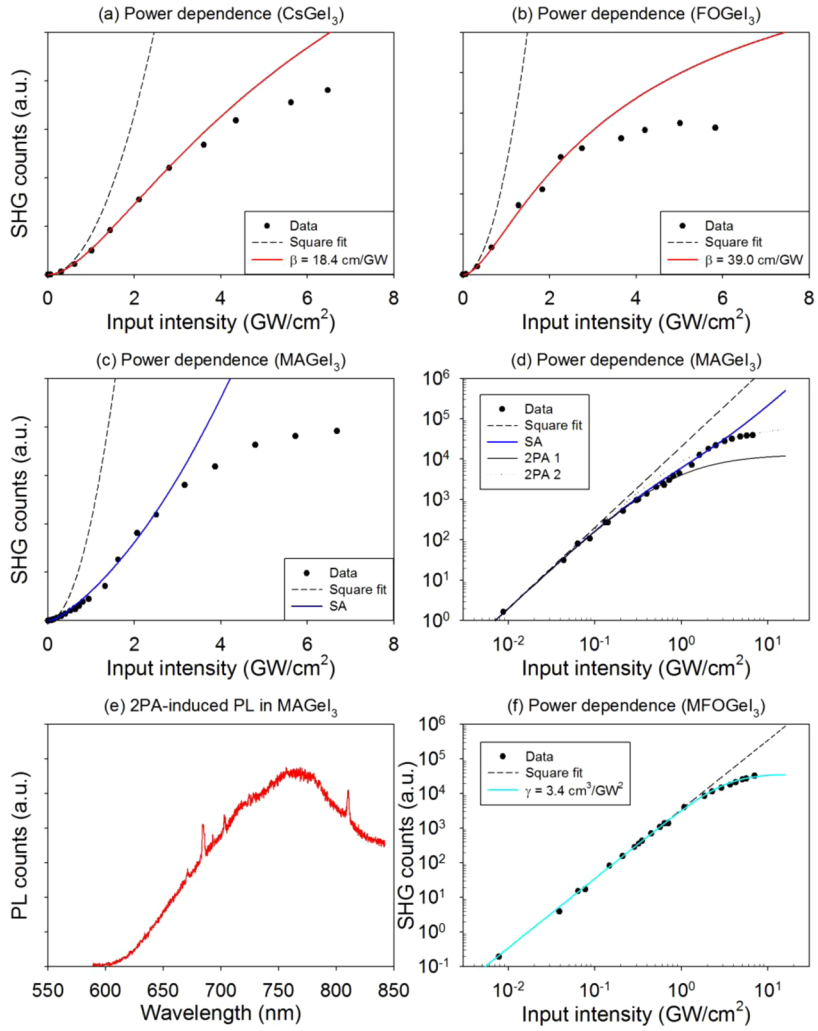

Figure 7. SHG power dependence (dots) of (a) $CsGeI_3$, (b) $FOGeI_3$ at λ = 1064 nm, respectively, superimposed by square fits (dashed) and 2PA fits (red). SHG power dependence of $MAGeI_3$ (dots) plotted on (c) linear scale and (d) log−log scale, respectively, with SA fits (blue). Two exemplary 2PA fits are shown in (d). (e) 2PA-induced PL (red) in $MAGeI_3$ at I = 0.5 GW/cm^2. (f) SHG power dependence (dots) of $MFOGeI_3$ superimposed by the square fit (dashed) and the 3PA fit (cyan).

counts is apparent near 750 nm and below, which is consistent with its band gap of E_g = 1.6 eV (775 nm). Also, a slight decrease between 1000−1150 nm can be attributed to linear absorption of the fundamental beam due to the capillary tube.[39] In fact, this effect is all common to our materials of investigation but does not affect our NLO analysis. We expect that the SHG response will approach a static value for λ in a typical mid-IR range, as indicated by the dashed lines.[40] The red traces in Figure 5b−e correspond to the SHG spectra from $MAGeI_3$, $FOGeI_3$, $MFOGeI_3$, and $AgGaS_2$ under the same experimental conditions. Again, a sharp drop was observed in the SHG counts near the band gap of each compound. All compounds containing organic cations showed noticeably reduced SHG responses at $\lambda/2$ = 750−800 nm and $\lambda/2$ > 1000 nm. For example, the SHG counts plummet at λ = 2100 and 2000 nm for $MAGeI_3$ and $FOGeI_3$, respectively. In Figure 5b−d, the arrows indicate the spectral ranges in which linear absorption of the input beam in $MAGeI_3$, $FOGeI_3$ and $MFOGeI_3$ results in significant decreases in the observed SHG counts (Figure S6).

In general, if other parameters are equal, the SHG coefficient $\chi^{(2)}$ decreases with increasing E_g ($\chi^{(2)} \propto 1/E_g^{3/2}$, Miller's rule)[41] as has been observed in most materials. However, for materials with similar band gaps, the degree of polar character in the structure plays the determining role. The three perovskite compounds reported here can be divided into two groups based on bandgap size. One group has a narrower E_g defined by $CsGeI_3$ (1.6 eV) and the other group defined by $MAGeI_3$ and $FOGeI_3$ has a much wider E_g (1.9 and 2.2 eV). Therefore, the SHG coefficient of the latter should be lower. However, $MAGeI_3$ and $FOGeI_3$ exhibit much higher SHG efficiencies in their transparent regions. This suggests that the origin of higher SHG in these compounds lies in the degree of polar character in the structure. As discussed above, the degree of distortion (g-parameter) is greater in $MAGeI_3$ and $FOGeI_3$ than in $CsGeI_3$ (Figure 3c). Thus, incorporation of organic cations into the $[GeI_3]^{1-}$ perovskite framework presumably enhances the optical matrix elements (stronger SHG dipole moments) as well as the joint density of states.[42] Although this is a plausible and intuitive interpretation of the observed trends in these three perovskites, a more quantitate analysis must await a proper theoretical treatment using state of the art calculation methods. The significantly reduced SHG efficiency of $MFOGeI_3$ with E_g = 2.5 eV, on the other hand, is attributed

DOI: 10.1021/jacs.5b01025
J. Am. Chem. Soc. 2015, 137, 6804−6819

to the dramatic change in the crystal structure induced by the 4-atom cation. As opposed to $MAGeI_3$ and $FOGeI_3$ which contain 2- and 3-atom cations, respectively, the 4-atom cation $MFOGeI_3$ adopts a non-perovskitic structure. The broadband SHG responses from $AGeI_3$ and $AgGaS_2$ are semilogarithmically plotted in Figure 5f for comparison.

Figure 6 shows the particle size dependence of the SHG counts from (a) $CsGeI_3$, (b) $MAGeI_3$, (c) $FOGeI_3$, (d) $MFOGeI_3$, and (e) $AgGaS_2$ at λ = 1800 nm, in which all samples and the reference materials are transparent. The observed size dependence is in fact typical of the type-I phase-matching case. Therefore, we can use the data of Figure 5 to estimate the absolute value of $\chi_S^{(2)}$ of the sample based on direct comparison with the reference value of $AgGaS_2$; $\chi_R^{(2)}$ = 36 pm/V;[43]

$$\chi_S^{(2)} = \chi_R^{(2)} \left| \frac{I_S(2\omega)}{I_R(2\omega)} \right|^{1/2} \quad (1)$$

Although compound **2** has some significant linear absorption ranges as shown in Figure 5b, we confirmed that it exhibits the strongest NLO response near λ = 1800 nm among the four compounds. On the basis of the dashed lines in Figure 5 and using eq 1, we estimated the SHG coefficients of the samples; $CsGeI_3$, $\chi_S^{(2)}$ = (125.3 ± 10.5) pm/V; $MAGeI_3$, $\chi_S^{(2)}$ = (161.0 ± 14.5) pm/V; $FOGeI_3$, $\chi_S^{(2)}$ = (143.0 ± 13.5) pm/V and $MFOGeI_3$, $\chi_S^{(2)}$ = (57.2 ± 5.5) pm/V, respectively. Our experimental value for $CsGeI_3$ is consistent with the theoretical value of $\chi_S^{(2)}$ = 127 pm/V[20b] and we believe that our estimations are correct within a 10% error range. Within the hybrid compounds **2**–**4**, the magnitude of band gaps seems to explain the experimental trend of decreasing SHG coefficients.

It is important to note that our compounds **1**–**4** possess much larger $\chi_S^{(2)}$ values than the ones obtained for the lighter germanium halide perovskites such as $CsGeCl_3$ ($\chi_S^{(2)}$ = 1.2 pm/V) and $CsGeBr_3$ ($\chi_S^{(2)}$ = 24 pm/V)[38b] or $RbGeCl_3 \cdot xH_2O$ ($\chi_S^{(2)}$ = 0.14 pm/V).[44] In fact, they join the family of the record-holding wide-gap compounds $KPSe_6$ ($\chi_S^{(2)}$ = 142.8 pm/V ± 10.5),[45] and γ-$NaAsSe_2$ ($\chi_S^{(2)}$ = 337.9 pm/V).[13b]

4. Laser-Induced Damage Threshold (LIDT) Determination. To further elucidate the properties of the compounds, we have estimated the LIDTs of **1**–**4** by varying the input pulse intensity at the Nd:YAG line in the powdered samples. Although typical LIDT measurements require a test material in a bulk form, the powder method is also well established.[46] The dots in Figure 7a correspond to the spectrally integrated SHG counts from $CsGeI_3$ when the input intensity was varied within our experimental range. The dashed curve represents the maximum SHG case in which fundamental depletion is absent, i.e., $I_{SHG} = aI^2$, where I_{SHG} and I are the SHG and fundamental intensities with a being a proportionality constant that incorporates $|\chi^{(2)}|^2$. The constant a was carefully determined by fitting the low-intensity regime where multiphoton absorption (MPA) is minimal. Note that the measured SHG counts deviate from the dashed curve for I > 0.6 GW/cm^2, indicating that the fundamental beam undergoes significant depletion. Considering the band gap of $CsGeI_3$ (E_g = 1.6 eV), the leading order process is two-photon absorption (2PA) that is characterized by a 2PA coefficient, β. We estimated β by fitting the measured SHG power dependence based on a modified fundamental intensity by 2PA, I_{2PA}:

$$I_{SHG} = aI_{2PA}^2, \quad \text{with} \quad I_{2PA} = \frac{I}{1 + \beta I d'} \quad (2)$$

where d = 125–150 μm is roughly the particle size for our reflection-based collection geometry.[14e,40] The red curve in Figure 7a is a fit using eq 2 with β = 18.4 cm/GW. This value is consistent with a typical two-band model at $x = \hbar\omega/E_g$:[40,47]

$$\beta(x) = K \frac{\sqrt{E_0}}{n_0^2 E_g^3} \frac{(2x-1)^{3/2}}{(2x)^5} \quad (3)$$

where K and E_0(~21 eV for direct-gap semiconductors) are the material-independent constants, $n_0 \sim 2.78$ is the static refractive index obtained by $n_0^4 E_g \sim 95$ eV,[48] and x is the dispersion parameter. The theoretical value of the Kane parameter K can range from 1940 to 5200 in units such that β is in cm/GW.[40] The best fit to our data yields K = 2700.

We still note that the observed SHG counts deviate from the red curve for I > 3 GW/cm^2. Since optical damage essentially occurs due to significant 2PA in $CsGeI_3$, we can assign the LIDT to the experimental intensity of 3 GW/cm^2. The value is typical for picosecond laser pulses.[49] Figure 7b shows the case for $FOGeI_3$ (E_g = 2.2 eV). The red curve yields β = 30.0 cm/GW, which is noticeably higher than a theoretical prediction given by eq 3; note that $\beta \propto E_g^{-3}$ with a minor x dependence for x > 0.8 or so. This could arise from the hybrid organic/inorganic nature of the compound since the parameters for the two-band model were exclusively determined for inorganic materials. The LIDT of $FOGeI_3$ is similar to that of $CsGeI_3$. Since the data collection times were different for the two samples due to the different SHG response of $CsGeI_3$ and $FOGeI_3$ at $\lambda/2$ = 532 nm, the relative SHG counts in Figure 7a, b do not indicate the same scales. The relative SHG efficiencies of the compounds at this wavelength are consistent with the previous data at λ_{SHG} = 550 nm, discussed above (see Figure 6a, c).

We found that $MAGeI_3$ exhibits a rather unusual SHG power dependence as shown in Figure 7c, d. This behavior is best illustrated by Figure 7d plotted on a log–log scale. The power dependence cannot be explained by a single 2PA fit (see 2PA-1 and 2PA-2 panels in Figure 7d). This behavior was confirmed several times by independent experiments. First, for I < 0.1 GW/cm^2, the SHG counts are well explained by $I_{SHG} = aI^2$ as expected. For 0.1 GW/cm^2 < I < 0.7 GW/cm^2, fundamental depletion by 2PA was observed, but the compound shows electronically induced transparency or saturable absorption (SA) as indicated by a square-law tendency for 0.7 GW/cm^2 < I < 3.0 GW/cm^2: The slope is rather parallel to the dashed line.

To fit the overall trend, we modified the 2PA coefficient by incorporating SA:

$$I_{SHG} = aI_{2PA}^2, \quad \text{with} \quad I_{2PA} = \frac{I}{1 + \beta I d/(1 + I/I_S)'} \quad (4)$$

where I_s is a parameter known as the saturation intensity. For I < I_s, the power dependence is similar to eq 2, but it follows the square behavior due to $I_{2PA} \propto I$ for I > I_s. The blue traces in Figure 7c, d are a fit using eq 4, yielding β = 91.0 cm/GW and I_s = 2.0 GW/cm^2. Note that the experimental data points deviate from the blue curve for I > 3 GW/cm^2, which corresponds to the LIDT.

Interestingly, we found that $MAGeI_3$ exhibits strong room-temperature photoluminescence (PL) under Nd:YAG pumping

DOI: 10.1021/jacs.5b01025
J. Am. Chem. Soc. 2015, 137, 6804–6819

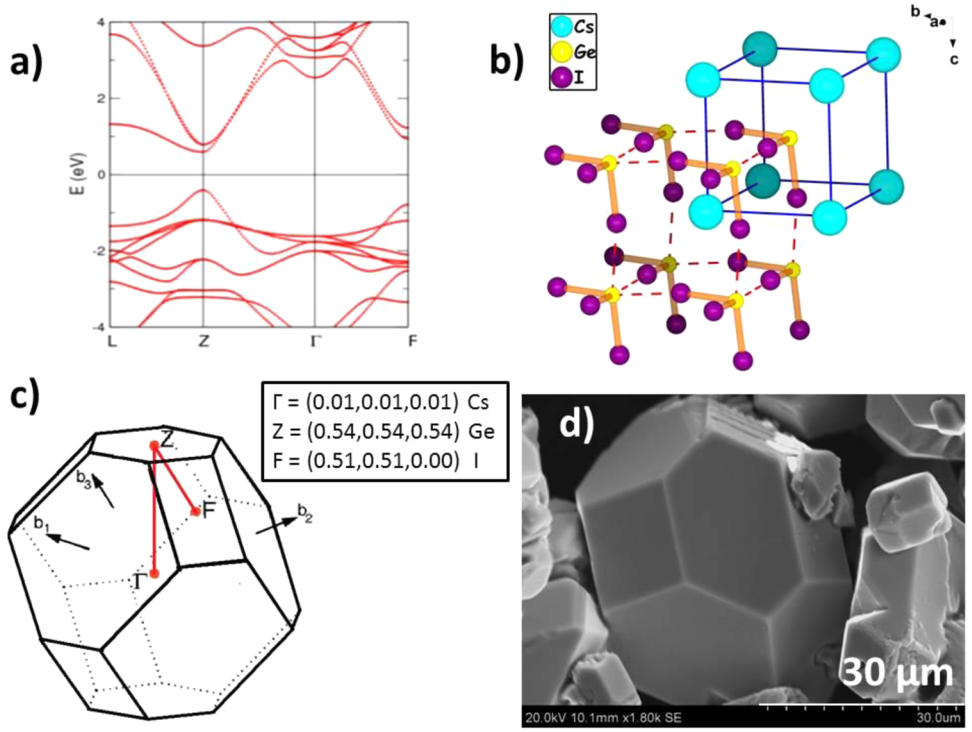

Figure 8. (a) Calculated band structure of $CsGeI_3$. (b) The relaxed crystal structure of $CsGeI_3$ in the reduced rhombohedral unit cell used for the calculations (blue rectangle). (c) A generic representation of the reciprocal unit cell of the rhombohedral cell describing **1**−**3**.[51] (d) SEM picture of an actual crystal of $CsGeI_3$ adopting a crystal habit reminiscent of the reduced unit cell.

via efficient 2PA. The PL can be visually detected as an apparently red emission, together with green SHG radiation (532 nm). The red trace in Figure 7e is the time-integrated PL at I = 0.5 GW/cm^2. We found that the high-wavelength end of the PL extends up to 950 nm, although it is significantly masked by the sideband of the fundamental beam, and therefore not shown here. Two minor sharp peaks are glitches when the CCD-range-scan windows overlap.

The dots in Figure 7f correspond to the observed SHG counts from $MFOGeI_3$. The dashed curve again represents the maximum SHG intensity. Note that the measured SHG counts increase with the square law up to I = 1.0 GW/cm^2. The deviation for higher intensities arises from three-photon absorption (3PA); note that the band gap of $MFOGeI_3$ (E_g = 2.5 eV) falls on the 3PA band. We estimated the corresponding 3PA coefficient γ by fitting the measured SHG power dependence based on a modified fundamental intensity by 3PA, I_{3PA}:

$$I_{SHG} = aI_{3PA}^2, \quad \text{with} \quad I_{3PA} = \frac{I}{[1 + 2\lambda I^2 d]^{1/2}} \tag{5}$$

The cyan curve in Figure 7f is a fit using eq 5 with γ = 3.4 cm^3/GW^2. This value is higher than typical 3PA coefficients of inorganic materials having similar band gaps.[50] Since the data points are well explained by the 3PA fit, we estimate that no significant optical damage occurs for $MFOGeI_3$ within our experimental range.

5. Electronic Structure Calculations. To complement our experimental work, theoretical calculations were carried out for **1**−**4**. $CsGeI_3$ was treated as having a true *R*3*m* symmetry, while $MAGeI_3$ and $FAGeI_3$ were approximated to have a monoclinic unit cell with a *Cm* space group symmetry. For computational simplicity, the monoclinic unit cells were approximated to rhombohedral symmetry with a *R*3*m* space group symmetry (Figure 8), while for $MFOGeI_3$, the monoclinic $P2_1$ symmetry was used. The original lattice parameters differ from the rhombohedral ones by less than 1% in angles. As shown in Figure 8b, where the rhombohedral unit cell of $CsGeI_3$ is depicted as an example, all compounds consist of the pyramidal $[GeI_3]^-$ unit, and the Cs^+ or the organic cations are located inside the $[Ge_4I_{12}]^{4-}$ perovskite box. Similar structural considerations apply for $MAGeI_3$ and $FOGeI_3$, while $MFOGeI_3$ has been treated independently (see Figure 1 for comparisons).

Calculated and experimental band gaps are listed in Table 5. Calculated band gaps are smaller than the experimental ones due to the well-known LDA band gap underestimation. In Figure 8, the electronic structure of $CsGeI_3$ is presented, whereas the full listing of the calculated band-structure plots are shown in Figure 9. **1**−**3** exhibit qualitatively similar behavior while the fine details are tuned by the nature of the A cation from Cs to MA and FO. The band structure of $MFOGeI_3$, which has a different unit cell, displays a distinctively different

Table 5. Experimental and Calculated Band Gaps and SHG Coefficients for 1−4[a]

compound	$E_{g,(exp)}$ (eV)	$E_{g,(cal)}$ (eV)	$\chi^{(2)}_{(exp)}$ (pm/V)
$CsGeI_3$ (**1**)	1.60	1.00	125.3 ± 10.5
$MAGeI_3$ (**2**)	1.90	1.17	161.0 ± 14.5
$FOGeI_3$ (**3**)	2.20	1.34	143.0 ± 13.5
$MFOGeI_3$ (**4**)	2.50	1.94	57.2 ± 5.5
$CsGeCl_3$[20b,38b]	3.67	2.26	1.2
$CsGeBr_3$[20b,38b]	2.32	1.49	24
$RbGeCl_3{\cdot}xH_2O$[44]	3.84	4.2	0.14

[a]Literature data for $CsGeCl_3$, $CsGeBr_3$, and $RbGeCl_3{\cdot}xH_2O$ are listed here for comparison.

DOI: 10.1021/jacs.5b01025
J. Am. Chem. Soc. 2015, 137, 6804−6819

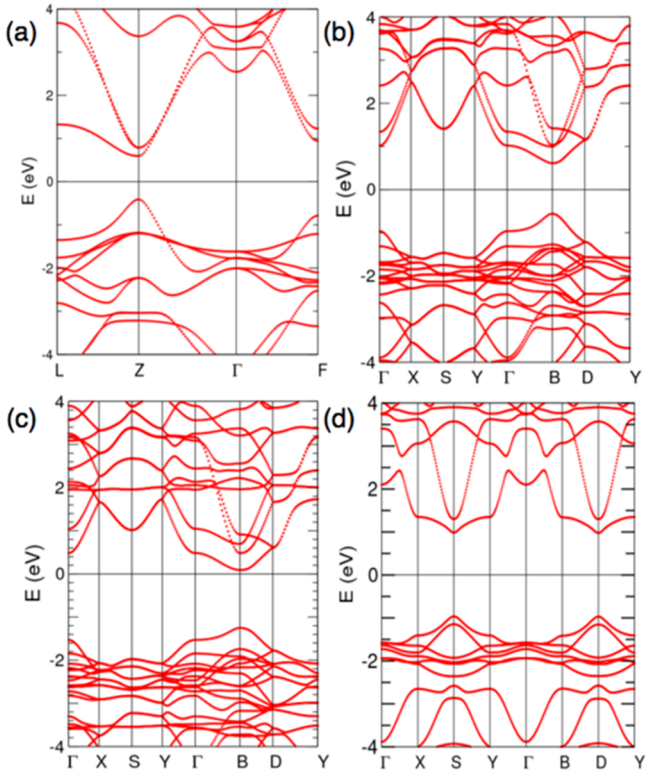

Figure 9. Electronic band structures of **1**–**4**: (a) $CsGeI_3$ (**1**), (b) $MAGeI_3$ (**2**), (c) $FOGeI_3$ (**3**), and (d) $MFOGeI_3$ (**4**).

character. In $CsGeI_3$, the valence band maximum (VBM) and the conduction band minimum (CBM) occur at the Z point, whereas in $MAGeI_3$ and $FOGeI_3$, the corresponding VBM and CBM extrema occur at the B point. An increase in the band gap is evident from **1**–**3** with the corresponding direct band gap values being 1.00, 1.17, and 1.34 eV, respectively (Figure 9a–c). On the other hand, in $MFOGeI_3$, VBM and CBM occur at the S and D points (Figure 9d) with a direct band gap of 1.94 eV and a relatively flat dispersion in both band edges compared to **1**–**3**.

Both VBM and CBM have a strong *p*-like orbital character originating from the Ge and I atoms in **1**–**4**. The dominance of I and Ge *p* states at VBM and CBM is manifested in the partial density of states (PDOS) plots in Figure 10 for compound **2** and Figures S7–S9 for $CsGeI_3$, $FOGeI_3$, and $MFOGeI_3$. States around the valence and conduction band edges are mainly composed of Ge and I *p* orbitals; hence, optical properties or SHG coefficients are mainly dictated by the Ge and I *p* states, whereas states from Cs, C, N, and H are either far away from VBM or CBM (as in $CsGeI_3$ and $MAGeI_3$) or otherwise weakly contributing (as in $FOGeI_3$ and to a lesser extent in $MFOGeI_3$). In **1**–**4** compounds, an *sp* hybridization of Ge and I is observed in both bonding and antibonding states which span from approximately −5.0 to 0.5 eV in the populated states as well as in the empty states. The Cs^+ ion in compound **1** displays a negligible degree of hybridization with the *s* and *p* states, while its main peak lies well below the bonding states.

Replacement of Cs^+ with organic cations in compounds **2**–**4** results in small changes in the DOS, as shown in the PDOS of $MAGeI_3$ for the C, H, and N atoms. In all three compounds, PDOS of C and H atoms are well localized near approximately −6 to −5 eV (similar to the Cs^+ ion), whereas the PDOS of N atoms shows significant variation among the three compounds.

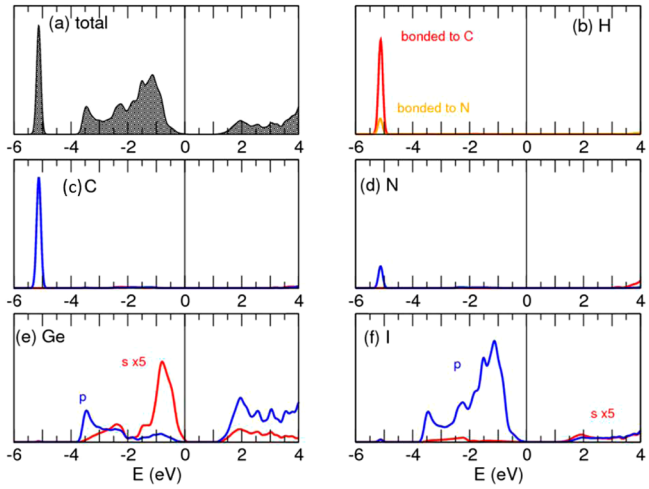

Figure 10. Density of states (DOS) of $MAGeI_3$. (a) Total DOS, contributions from (b) H (1,2), (c) C, (d) N, (e) Ge, and (f) I. Red and blue lines denote *s* and *p* orbital contributions, respectively. Some PDOS are multiplied by 5 for better illustration.

While the N *p* orbitals localization occurs at similar energies as for C and H atoms in $MAGeI_3$ and $MFOGeI_3$, in compound **3** the N *p* orbitals exhibit a stronger hybridization interaction with the Ge and I states. The PDOS of Ge and I themselves is also affected by the Cs substitution. The general shape of I *p* bands is not significantly affected by the organic cation replacement, yet the relative position of the VBM is shifted to higher energies. Similarly, the corresponding Ge *s* bands remain practically unchanged and mainly the Ge *p* bands are affected as the cation changes, shifting the CBM to higher energies. Overall, the dominance of *p* states in occupied states is preserved in **1**–**4**, but a significant shift toward higher energies is observed for both CBM and VBM extrema, a trend which is responsible for the significant increase of the experimental band gaps.

CONCLUSIONS

A broad and structurally diverse family of polar hybrid, organic/inorganic, medium-to-wide gap semiconductors based on the trigonal pyramidal $[GeI_3]^-$ building block can be prepared by utilizing a simple and scalable solution technique. We have found that the incremental change in the size of the small organic cations results in large changes in the self-assembly of the $[GeI_3]^-$ units resulting in a variety of perovskite crystal structures within the $AGeI_3$ family. The incorporation of the small polar organic molecule in place of Cs ions has a dramatic effect in the electronic structure of the semiconductors introducing a large opening of the band gap as the cation size increases even within the same structure type. Due to this effect, the compounds exhibit a large SHG response, which in the cases of $MAGeI_3$ and $FOGeI_3$ surpasses the best performing halogermanate SHG material $CsGeI_3$. In addition, the compounds possess relatively large LIDTs, which in the case of $MFOGeI_3$ may exceed 3 GW/cm^2 while outperforming the commercially employed $AgGaS_2$ compound in the SHG conversion efficiency. The enhancement of the SHG conversion efficiency reported here is attributed to the polar nature of the cations as shown by both experimental and theoretical evidence. Although some absorption in the mid-IR range present for **1**–**4** due to molecular vibrations of the organic ions could be potentially problematic, the compounds

DOI: 10.1021/jacs.5b01025
J. Am. Chem. Soc. 2015, 137, 6804–6819

could be utilized for NLO applications in the visible and near-IR regions due to phase-matchability, high SHG conversion efficiencies and high LIDTs. In addition, the hybrid organic/inorganic nature of the compounds renders them solution processable and therefore amenable to technological exploitation in thin films and devices. This work opens a path for a more general application of the small organic cation substitution approach in other polar compounds, in order to engineer similar enhancement effects both in band gap and SHG conversion efficiency. State-of-the art SHG materials such as the phosphate and the borate semiconductors, among others, appear as excellent candidates in targeting a new generation of hybrid SHG conversion materials.

■ ASSOCIATED CONTENT

Supporting Information

Supporting Information for this manuscript includes the crystallographic files of compounds **1**−**7** in .cif format. Complementary details on the experimental methods, powder XRD patterns, IR spectra, extra material related with the SHG experiments and electronic structure calculations and full listing of crystallographic and DOS calculations data. The Supporting Information is available free of charge on the ACS Publications website at DOI: 10.1021/jacs.5b01025.

■ AUTHOR INFORMATION

Corresponding Author

*m-kanatzidis@northwestern.edu

Notes

The authors declare no competing financial interest.

■ ACKNOWLEDGMENTS

The work was supported by grant SC0012541 from the U.S. Department of Energy, Office of Science. Sonny H. Rhim thanks the Department of Homeland Security under Award No 2010-DN-077-ARI042-02. Y.S.K. acknowledges support from the Basic Research Lab Program (2014R1A4A1071686) and Priority Research Center Program (2009-0093818) through the NRF of Korea funded by the Ministry of Education and Ministry of Science, ICT and Future Planning. L.F. was supported by NSF IGERT DGE-0801685.

■ REFERENCES

(1) Chung, I.; Lee, B.; He, J.; Chang, R. P. H.; Kanatzidis, M. G. *Nature* **2012**, *485*, 486.
(2) (a) Lee, M. M.; Teuscher, J.; Miyasaka, T.; Murakami, T. N.; Snaith, H. J. *Science* **2012**, *338*, 643. (b) Burschka, J.; Pellet, N.; Moon, S.-J.; Humphry-Baker, R.; Gao, P.; Nazeeruddin, M. K.; Gratzel, M. *Nature* **2013**, *499*, 316. (c) Liu, M.; Johnston, M. B.; Snaith, H. J. *Nature* **2013**, *501*, 395.
(3) Snaith, H. J. *J. Phys. Chem. Lett.* **2013**, *4*, 3623.
(4) Zhou, H.; Chen, Q.; Li, G.; Luo, S.; Song, T.-b.; Duan, H.-S.; Hong, Z.; You, J.; Liu, Y.; Yang, Y. *Science* **2014**, *345*, 542.
(5) Xing, G.; Mathews, N.; Lim, S. S.; Yantara, N.; Liu, X.; Sabba, D.; Grätzel, M.; Mhaisalkar, S.; Sum, T. C. *Nat. Mater.* **2014**, *13*, 476.
(6) Stoumpos, C. C.; Malliakas, C. D.; Peters, J. A.; Liu, Z.; Sebastian, M.; Im, J.; Chasapis, T. C.; Wibowo, A. C.; Chung, D. Y.; Freeman, A. J.; Wessels, B. W.; Kanatzidis, M. G. *Cryst. Growth Des.* **2013**, *13*, 2722.
(7) He, Y.; Galli, G. *Chem. Mater.* **2014**, *26*, 5394.
(8) (a) Jin, H.; Im, J.; Freeman, A. J. *Phys. Rev. B* **2012**, *86*, 121102. (b) Yang, K.; Setyawan, W.; Wang, S.; Buongiorno Nardelli, M.; Curtarolo, S. *Nat. Mater.* **2012**, *11*, 614.
(9) Kim, M.; Im, J.; Freeman, A. J.; Ihm, J.; Jin, H. *Proc. Natl. Acad. Sci. U.S.A.* **2014**, *111*, 6900.
(10) Nie, W. *Adv. Mater.* **1993**, *5*, 520.
(11) (a) Pantazis, P.; Maloney, J.; Wu, D.; Fraser, S. E. *Proc. Natl. Acad. Sci. U.S.A.* **2010**, *107*, 14535. (b) Franken, P. A.; Hill, A. E.; Peters, C. W.; Weinreich, G. *Phys. Rev. Lett.* **1961**, *7*, 118.
(12) Dmitriev, V. G., Gurzadyan, G. G., Nikogosyan, D. N. *Handbook of Nonlinear Optical Crystals*; 3rd rev. ed.; Springer-Verlag: Heidelberg, 1999; Vol. *64*.
(13) (a) Li, H.; Peters, J. A.; Liu, Z.; Sebastian, M.; Malliakas, C. D.; Androulakis, J.; Zhao, L.; Chung, I.; Nguyen, S. L.; Johnsen, S.; Wessels, B. W.; Kanatzidis, M. G. *Cryst. Growth Des.* **2012**, *12*, 3250. (b) Bera, T. K.; Jang, J. I.; Song, J.-H.; Malliakas, C. D.; Freeman, A. J.; Ketterson, J. B.; Kanatzidis, M. G. *J. Am. Chem. Soc.* **2010**, *132*, 3484. (c) Bera, T. K.; Jang, J. I.; Ketterson, J. B.; Kanatzidis, M. G. *J. Am. Chem. Soc.* **2009**, *131*, 75. (d) Bera, T. K.; Song, J.; Freeman, A. J.; Jang, J. I.; Ketterson, J. B.; Kanatzidis, M. G. *Angew. Chem., Int. Ed.* **2008**, *47*, 7828.
(14) (a) Banerjee, S.; Malliakas, C. D.; Jang, J. I.; Ketterson, J. B.; Kanatzidis, M. G. *J. Am. Chem. Soc.* **2008**, *130*, 12270. (b) Chung, I.; Song, J.; Jang, J. I.; Freeman, A. J.; Ketterson, J. B.; Kanatzidis, M. G. *J. Am. Chem. Soc.* **2009**, *131*, 2647. (c) Chung, I.; Jang, J. I.; Malliakas, C. D.; Ketterson, J. B.; Kanatzidis, M. G. *J. Am. Chem. Soc.* **2010**, *132*, 384. (d) Chung, I.; Malliakas, C. D.; Jang, J. I.; Canlas, C. G.; Weliky, D. P.; Kanatzidis, M. G. *J. Am. Chem. Soc.* **2007**, *129*, 14996. (e) Morris, C. D.; Chung, I.; Park, S.; Harrison, C. M.; Clark, D. J.; Jang, J. I.; Kanatzidis, M. G. *J. Am. Chem. Soc.* **2012**, *134*, 20733.
(15) Stoumpos, C. C.; Malliakas, C. D.; Kanatzidis, M. G. *Inorg. Chem.* **2013**, *52*, 9019.
(16) (a) Trots, D. M.; Myagkota, S. V. *J. Phys. Chem. Solids* **2008**, *69*, 2520. (b) Chung, I.; Song, J.-H.; Im, J.; Androulakis, J.; Malliakas, C. D.; Li, H.; Freeman, A. J.; Kenney, J. T.; Kanatzidis, M. G. *J. Am. Chem. Soc.* **2012**, *134*, 8579.
(17) (a) Thiele, G.; Rotter, H. W.; Schmidt, K. D. *Z. Anorg. Allg. Chem.* **1987**, *545*, 148. (b) Thiele, G.; Rotter, H. W.; Schmidt, K. D. *Z. Anorg. Allg. Chem.* **1989**, *571*, 60. (c) Tang, L.-C.; Chang, C.-S.; Huang, J. Y. *J. Phys.: Condens. Matter* **2000**, *12*, 9129.
(18) Rosker, M. J.; Cunningham, P. H.; Ewbank, M. D.; Gunter, P. (Boeing North American, Inc.) US005721634A, 1998.
(19) (a) Gu, Q. T.; Pan, Q. W.; Shi, W.; Sun, X.; Fang, C. S. *Prog. Cryst. Growth Charact. Mater.* **2000**, *40*, 89. (b) Gu, Q. T.; Fang, C. S.; Shi, W.; Wu, X. W.; Pan, Q. W. *J. Cryst. Growth* **2001**, *225*, 501. (c) Tang, L. C.; Huang, J. Y.; Chang, C. S.; Lee, M. H.; Liu, L. Q. *J. Phys.: Condens. Matter* **2005**, *17*, 7275. (d) Lin, Z. G.; Tang, L. C.; Chou, C. P. *J. Phys.: Condens. Matter* **2007**, *19*, No. 476209. (e) Lin, Z.-G.; Tang, L.-C.; Chou, C.-P. *J. Cryst. Growth* **2008**, *310*, 3224. (f) Lin, Z. G.; Tang, L. C.; Chou, C. P. *Opt. Mater.* **2008**, *31*, 28. (g) Lin, Z. G.; Tang, L. C.; Chou, C. P. *Inorg. Chem.* **2008**, *47*, 2362.
(20) (a) Tang, L. C.; Chang, Y. C.; Huang, J. Y.; Chang, C. S. In *Infrared and Photoelectronic Imagers and Detector Devices II*; Longshore, R. E., Sood, A., Eds.; SPIE-Int Soc Optical Engineering: Bellingham, 2006; Vol. *6294*, p J2940. (b) Tang, L. C.; Chang, Y. C.; Huang, J. Y.; Lee, M. H.; Chang, C. S. *Jpn. J. Appl. Phys.* **2009**, *48*, 112402. (c) Katan, C.; Pedesseau, L.; Kepenekian, M.; Rolland, A.; Even, J. *J. Mater Chem. A* **2015**, *3*, 9232.
(21) (a) Yamada, K.; Isobe, K.; Okuda, T.; Furukawa, Y. *Z. Naturforsch., A* **1994**, *49*, 258. (b) Yamada, K.; Isobe, K.; Tsuyama, E.; Okuda, T.; Furukawa, Y. *Solid State Ionics* **1995**, *79*, 152. (c) Mitzi, D. B. *Chem. Mater.* **1996**, *8*, 791. (d) Okuda, T.; Gotou, S.; Takahashi, T.; Terao, H.; Yamada, K. *Z. Naturforsch., A* **1996**, *51*, 686.
(22) Mikkelsen, J. J. C.; Kildal, H. *J. Appl. Phys.* **1978**, *49*, 426.
(23) Sheldrick, G. *Acta Crystallogr., Sect. A* **2008**, *64*, 112.
(24) Spek, A. *Acta Crystallogr., Sect. D* **2009**, *65*, 148.
(25) Farrugia, L. *J. Appl. Crystallogr.* **2012**, *45*, 849.
(26) (a) Aroyo, M. I.; Kirov, A.; Capillas, C.; Perez-Mato, J. M.; Wondratschek, H. *Acta Crystallogr., Sect. A* **2006**, *62*, 115. (b) Aroyo Mois, I.; Perez-Mato Juan, M.; Capillas, C.; Kroumova, E.; Ivantchev, S.; Madariaga, G.; Kirov, A.; Wondratschek, H. *Z. Kristallogr.* **2006**, *221*, 15.

DOI: 10.1021/jacs.5b01025
J. Am. Chem. Soc. 2015, 137, 6804−6819

(27) (a) Jansen, H. J. F.; Freeman, A. J. *Phys. Rev. B* **1984**, *30*, 561. (b) Wimmer, E.; Krakauer, H.; Weinert, M.; Freeman, A. J. *Phys. Rev. B* **1981**, *24*, 864.
(28) Hedin, L.; Lundqvist, B. I. *J. Phys. C: Solid State Phys.* **1971**, *4*, 2064.
(29) (a) Sipe, J. E.; Ghahramani, E. *Phys. Rev. B* **1993**, *48*, 11705. (b) Aversa, C.; Sipe, J. E. *Phys. Rev. B* **1995**, *52*, 14636. (c) Hughes, J. L. P.; Sipe, J. E. *Phys. Rev. B* **1996**, *53*, 10751. (d) Rashkeev, S. N.; Lambrecht, W. R. L.; Segall, B. *Phys. Rev. B* **1998**, *57*, 3905. (e) Rashkeev, S. N.; Lambrecht, W. R. L. *Phys. Rev. B* **2001**, *63*, 165212.
(30) (a) Kanatzidis, M. G.; Huang, S.-P. *Angew. Chem., Int. Ed. Engl.* **1989**, *28*, 1513. (b) Huang, S. P.; Kanatzidis, M. G. *Inorg. Chem.* **1991**, *30*, 1455. (c) Kanatzidis, M. G. *Phosphorus, Sulfur Silicon Relat. Elem.* **1994**, *93*, 159. (d) Kim, K.-W.; Kanatzidis, M. G. *J. Am. Chem. Soc.* **1998**, *120*, 8124.
(31) (a) Kortüm, G.; Braun, W.; Herzog, G. *Angew. Chem.* **1963**, *75*, 653. (b) McCarthy, T. J.; Tanzer, T. A.; Kanatzidis, M. G. *J. Am. Chem. Soc.* **1995**, *117*, 1294. (c) Larson, P.; Mahanti, S. D.; Kanatzidis, M. G. *Phys. Rev. B* **2000**, *61*, 8162. (d) Trikalitis, P. N.; Rangan, K. K.; Bakas, T.; Kanatzidis, M. G. *J. Am. Chem. Soc.* **2002**, *124*, 12255. (e) Larson, P.; Mahanti, S. D.; Kanatzidis, M. G. *Phys. Rev. B* **2000**, *61*, 8162.
(32) Ozisik, H.; Colakoglu, K.; Ozisik, H. B.; Deligoz, E. *Comput. Mater. Sci.* **2010**, *50*, 349.
(33) Tauc, J. *Mater. Res. Bull.* **1968**, *3*, 37.
(34) Novoselova, A. V.; Todriya, M. K.; Odin, I. N.; Popovkin, B. A. *Inorg. Mater.* **1971**, *7*, 1125.
(35) Nakamoto, K. *Infrared and Raman Spectra of Inorganic and Coordination Compounds*; 6th ed.; John Wiley & Sons Inc.: Hoboken, NJ, 2009.
(36) Kurtz, S. K.; Perry, T. T. *J. Appl. Phys.* **1968**, *39*, 3798.
(37) Canarelli, P.; Benko, Z.; Hielscher, A. H.; Curl, R. F.; Tittel, F. K. *IEEE J. Quantum Electron.* **1992**, *28*, 52.
(38) (b) Zhi-Guang, L.; Li-Chuan, T.; Chang-Pin, C. *J. Phys.: Condens. Matter* **2007**, *19*, 476209. (c) Lin, Z.-G.; Tang, L.-C.; Chou, C.-P. *J. Cryst. Growth* **2008**, *310*, 3224. (a) Yamada, K.; Mikawa, K.; Okuda, T.; Knight, K. S. *J. Chem. Soc., Dalton Trans.* **2002**, 2112.
(39) Haynes, A. S.; Saouma, F. O.; Otieno, C. O.; Clark, D. J.; Shoemaker, D. P.; Jang, J. I.; Kanatzidis, M. G. *Chem. Mater.* **2015**, *27*, 1837.
(40) Jang, J. I.; Park, S.; Harrison, C. M.; Clark, D. J.; Morris, C. D.; Chung, I.; Kanatzidis, M. G. *Opt. Lett.* **2013**, *38*, 1316.
(41) Jackson, A. G.; Ohmer, M. C.; LeClair, S. R. *Infrared Phys. Technol.* **1997**, *38*, 233.
(42) Song, J.-H.; Freeman, A. J.; Bera, T. K.; Chung, I.; Kanatzidis, M. G. *Phys. Rev. B* **2009**, *79*, 245203.
(43) Weber, M. J. *Handbook of Optical Materials*; CRC Press: Boca Raton, FL, 2002.
(44) Li-Chuan, T.; Li-Qiang, L.; Yia-Chung, C.; Jui-hsien, Y.; Jung-Yau, H.; Chen-Shiung, C. *Jpn. J. Appl. Phys.* **2009**, *48*, 082001.
(45) Jang, J. I.; Haynes, A. S.; Saouma, F. O.; Otieno, C. O.; Kanatzidis, M. G. *Opt. Mater. Express* **2013**, *3*, 1302.
(46) (a) Jang, J. I.; Clark, D. J.; Brant, J. A.; Aitken, J. A.; Kim, Y. S. *Opt. Lett.* **2014**, *39*, 4579. (b) Brant, J. A.; Clark, D. J.; Kim, Y. S.; Jang, J. I.; Weiland, A.; Aitken, J. A. *Inorg. Chem.* **2015**, *54*, 2809.
(47) (a) Sheik-Bahae, M.; Hutchings, D. C.; Hagan, D. J.; Van Stryland, E. W. *IEEE J. Quantum Electron.* **1991**, *27*, 1296. (b) Boyd, R. W. *Nonlinear Optics*; 3rd ed.; Academic Press: San Diego, CA, 2008.
(48) Ravindra, N. M.; Ganapathy, P.; Choi, J. *Infrared Phys. Technol.* **2007**, *50*, 21.
(49) Nikogosyan, D. N. *Nonlinear Optical Crystals: A Complete Survey*; 1st ed.; Springer-Verlag: New York, 2005.
(50) (a) Brandi, H. S.; Araujos, C. B. d. *J. Phys. C: Solid State Phys.* **1983**, *16*, 5929. (b) He, J.; Qu, Y.; Li, H.; Mi, J.; Ji, W. *Opt. Express* **2005**, *13*, 9235.
(51) Setyawan, W.; Curtarolo, S. *Comput. Mater. Sci.* **2010**, *49*, 299.

DOI: 10.1021/jacs.5b01025
J. Am. Chem. Soc. 2015, 137, 6804−6819